JGR Space Physics

RESEARCH ARTICLE
10.1029/2019JA027037

Key Points:
- X-lines, including the 11 July 2017 reconnection event, are reconstructed at and beyond 20 R_E, but for strong driving they can come closer
- Current sheets in the growth phase may be as thin as 0.2 R_E, and at the same time, as long as 15 R_E, violating isotropic force balance
- B_z humps form in the growth phase, and their reconfiguration may precede X-line formation and substorm onset

Supporting Information:
- Supporting Information S1

Correspondence to:
M. I. Sitnov,
Mikhail.Sitnov@jhuapl.edu

Citation:
Sitnov, M. I., Stephens, G. K., Tsyganenko, N. A., Miyashita, Y., Merkin, V. G., Motoba, T., et al. (2019). Signatures of nonideal plasma evolution during substorms obtained by mining multimission magnetometer data. *Journal of Geophysical Research: Space Physics*, *124*. https://doi.org/10.1029/2019JA027037

Received 13 JUN 2019
Accepted 23 SEP 2019
Accepted article online 12 OCT 2019

Signatures of Nonideal Plasma Evolution During Substorms Obtained by Mining Multimission Magnetometer Data

M. I. Sitnov[1], G. K. Stephens[1], N. A. Tsyganenko[2], Y. Miyashita[3], V. G. Merkin[1], T. Motoba[1], S. Ohtani[1], and K. J. Genestreti[4]

[1]Applied Physics Laboratory, The Johns Hopkins University, Laurel, MD, USA, [2]Institute and Department of Physics, Saint Petersburg State University, Saint Petersburg, Russia, [3]Korea Astronomy and Space Science Institute, Daejeon, South Korea, [4]Space Science Center, University of New Hampshire, Durham, NH, USA

Abstract Substorm-type evolution of the Earth's magnetosphere is investigated by mining more than two decades (1995–2017) of spaceborne magnetometer data from multiple missions including the first two years (2016-2017) of the Magnetospheric MultiScale mission. This investigation reveals interesting features of plasma evolution distinct from ideal magnetohydrodynamics (MHD) behavior: X-lines, thin current sheets, and regions with the tailward gradient of the equatorial magnetic field B_z. X-lines are found to form mainly beyond 20 R_E, but for strong driving, with the solar wind electric field exceeding ~ 5mV/m, they may come closer. For substorms with weaker driving, X-lines may be preceded by redistribution of the magnetic flux in the tailward B_z gradient regions, similar to the magnetic flux release instability discovered earlier in PIC and MHD simulations as a precursor mechanism of the reconnection onset. Current sheets in the growth phase may be as thin as 0.2 R_E, comparable to the thermal ions gyroradius, and at the same time, as long as 15 R_E. Such an aspect ratio is inconsistent with the isotropic force balance for observed magnetic field configurations. These findings can help resolve kinetic mechanisms of substorm dipolarizations and adjust kinetic generalizations of global MHD models of the magnetosphere. They can also guide and complement microscale analysis of nonideal effects.

Plain Language Summary The sun emits a steam of charged particles called the solar wind that flows past the Earth interacting with the planet's dipole magnetic field. This stretches the dipolar magnetic field away from the sun on the nightside of the planet storing energy in the stretched field. Once every few hours, this stretched configuration suddenly becomes more dipolar bringing particles and magnetic flux closer to the planet and powering aurora in the polar regions. During these processes, termed substorms, the gas of charged particles, protons, and electrons trapped by the dipole and known as plasma, behaves largely as a perfectly conducting fluid. However, only deviations from this ideal conducting plasma behavior can explain the substorm mechanisms. We mine two decades of spacecraft magnetometer data from multiple missions to form swarms of thousands of synthetic probes. They help reveal effects of nonideal plasma evolution during substorms, which cannot be captured by direct in situ observations because of their extreme paucity.

1. Introduction

The Earth's magnetic field carves out a gigantic cavity known as the magnetosphere in the flow of supersonic and super-Alfvenic magnetized solar wind plasma. The magnetosphere is composed of practically collisionless plasmas (with the Lundquist number $S \sim 4 \cdot 10^{15}$ (Ji & Daughton, 2011) for typical conditions (Kivelson & Russell, 1995)). In such an ideal, perfectly conducting system the magnetic field lines must be frozen into the plasma fluid and move along with it (Alfvén, 1942). Therefore the magnetosphere can be expected to be well described by the equations of ideal magnetohydrodynamics (MHD) (e.g., Lyon et al., 2004). Indeed, many aspects of magnetospheric dynamics are successfully reproduced by global MHD models (e.g., Gordeev et al., 2015).

However, more than half a century ago, while examining the magnetospheric convection cycle, Dungey (1961) concluded that there are regions with topological singularities of the magnetic field, where ideal MHD

conditions must be violated in the solar wind-magnetosphere system. First, the interaction of the magnetosphere with the solar wind should result in the appearance of X-lines at the dayside magnetopause, and, at least for southward Interplanetary Magnetic Field (IMF), in the magnetotail. Near X-lines the magnetic field becomes zero, making plasma particles unmagnetized and hence plasma is not frozen into the magnetic field. As a result, in the vicinity of an X-line, one can expect a special nonideal MHD behavior of plasma called magnetic reconnection (Galeev, 1984). Even in the more complex case of guide field reconnection (e.g., Fuselier et al., 2011), one can expect particle acceleration along the X-line and hence nonideal effects (Burch & Phan, 2016).

New X-lines may appear in the tail during disturbed periods, such as substorms, and since long ago, magnetic reconnection is reasonably considered as the main driving mechanism for substorms (Hones, 1979). The formation and evolution of X-lines, plasmoids, and flux ropes has been firmly established by in situ observations of Geotail, Cluster, Time History of Events and Macroscale Interactions during Substorms (THEMIS), Acceleration, Reconnection, Turbulence and Electrodynamics of the Moons Interaction with the Sun (ARTEMIS) and Magnetospheric MultiScale (MMS) missions (Angelopoulos et al., 2013; Eastwood et al., 2010; Ieda et al., 1998; Li et al., 2014; Torbert et al., 2018). However, systematic observations of the formation and evolution of X-lines in the magnetotail, necessary to understand their formation mechanisms and their role in substorms, remain a very difficult task (McPherron, 2016) generally because of data paucity and specifically because of infrequent appearance of X-lines within $20R_E$ (R_E is the Earth radius) (Baumjohann et al., 1990) and even beyond that distance (yet within $31R_E$; Ohtani & Mukai 2008). In particular, in the process of several-month dedicated MMS observations of magnetic reconnection in summer 2017, only a few cases featuring electron diffusion regions (EDRs) have been reported so far (Chen et al., 2019; Torbert et al., 2018).

Another significant deviation from the ideal-MHD picture, which may appear already in the substorm growth phase, is the formation of thin current sheets (TCSs). Scanning cross-tail structure due to the tail current sheet (CS) flapping motions (e.g., Sergeev et al., 1993), remote-sensing methods (Sergeev et al., 2018), and multiprobe observations (e.g., Runov et al., 2008) showed that TCSs with the half-thickness $L_z^{(TCS)} \lesssim 0.2R_E \sim \rho_{0i}$, where ρ_{0i} is the thermal ion gyroradius in the field B_0 outside the TCS, form prior to substorm onset. A TCS can be embedded into a thicker plasma sheet with much smaller current density or form bifurcated structures (e.g., Asano et al., 2005). An important feature of TCSs is not only their kinetic (ion-scale) thickness and complex multiscale structure but also their relatively large extension L_x in the radial direction. For example, multispacecraft observations by Pulkkinen et al. (1998) using GOES-8, GOES-9 and Geotail data, suggest that prior to the substorm onset, the TCS may extend from the quasi-dipolar to the midtail region and hence their radial extension may reach $\sim 20R_E$. The global nature of CS thinning and stretching prior to the substorm onset is also seen from a superposed epoch analysis of substorms (Miyashita et al., 2009, Figures 2 and 7) as a decrease of the northward magnetic field B_z and increase of the total pressure in the premidnight sector ($2R_E < y < 12R_E$ and $-20R_E < x < -5R_E$). An even more audacious hypothesis that TCSs may occupy the entire tail from near-Earth region to lunar orbit has recently been proposed by Artemyev et al. (2019) based on GOES-15, THEMIS, and ARTEMIS observations.

At the same time, analysis of self-consistent tail current sheet equilibria (Sitnov & Merkin, 2016) suggests that in an isotropic CS with realistic values of the normal magnetic field $B_z \geq 0.03B_0$, the current sheet thickness $L_z(x)$ at distances $L_x \sim 10^2 L$, where L is the CS thickness near the Earth, becomes too large $L_z \sim L\exp(L_x/L)(B_z/B_0) > 20L$ for it to maintain a kinetic scale. This is consistent with original estimates of the magnetotail force balance (Cole & Schindler, 1972; Rich et al., 1972) suggesting that balancing the magnetic tension by an isotropic plasma pressure gradient requires the current sheet aspect ratio to be close to the magnetic field stretching factor $L_x/L \cong B_0/B_z$. Recent direct estimates of the force balance along the tail (Artemyev et al., 2015) indicate that the TCS properties may indeed be different from isotropic and gyrotropic plasma models. These deviations from MHD may be critical for the reconnection onset mechanism in the magnetotail (e.g., Zelenyi et al., 2008). Thus, assessing the extension of TCSs in the equatorial plane is fundamentally important for understanding their possible nonideal nature.

Yet another interesting and potentially non-MHD feature is the formation of a tailward gradient region (TGR) of the equatorial magnetic field component B_z. Having been extensively discussed before as a characteristic feature of the Steady Magnetospheric Convection (SMC) events (e.g., Sergeev et al., 1996), TGRs recently gained new interest as a necessary condition for spontaneous reconnection onset (Sitnov &

Schindler, 2010) provided by the so-called ion tearing instability (Schindler, 1974). TGRs should not survive in the steady-state ideal MHD case because they are also unstable with respect to ballooning/interchange perturbations. Moreover, their instability threshold in ideal regimes is the lowest compared to any other MHD modes (Schindler & Birn, 2004). Hence it must be lower compared to the ideal/initial regimes of tearing (Merkin & Sitnov, 2016; Sitnov et al., 2019). At the same time, the formation of TGRs in the late growth phase is suggested by statistical visualization of substorms (Machida et al., 2009; Wang et al., 2004), remote-sensing studies (Sergeev et al., 2018), and by first results of a substorm reconstruction with a data-mining (DM) approach (Stephens et al., 2019).

In contrast to X-lines whose nonideal nature is obvious, the nonideal nature of TCSs and TGRs is not guaranteed. For example, the formation of a TGR may be an integral effect of many meso-scale earthward flows, as is the case in some MHD simulations of SMC regimes (Garcia-Sage et al., 2016). Similarly, the detection of TCSs in different regions of the magnetotail (e.g., Pulkkinen et al., 1998) does not rule out the possibility that the TCS structure in the equatorial plane is patchy and thus still consistent with isotropic ideal MHD. For example, localized TCS may appear because of magnetotail boundary deformations (Birn et al., 2003). Still, for clarity we use the term "nonideal" hereafter to describe collectively X-lines, TCSs, and TGRs, with this caveat in mind, because they all at least potentially violate the ideal isotropic MHD description of the magnetosphere.

All of these nonideal regimes are difficult to visualize in a global context because global models generally lack the necessary physical prescriptions to reproduce them. In this paper, we use the DM method described recently by Stephens et al. (2019) to derive such a global context and show where and when X-lines, TCSs, and TGRs form during various phases of observed substorms.

X-lines, TCSs, and TGRs do not exhaust the range of non-MHD effects in the magnetosphere of which the most well known is the storm-time ring current provided by the energy dependent drifts of hot plasma populations in the inner magnetosphere (Wolf, 1983). While these effects can also be captured by the method described below, many of them were already discussed in earlier investigations of storms (Sitnov et al., 2008, 2010; Stephens et al., 2016) and storm-scale effects of substorms (Stephens et al., 2019). Thus, the present study largely complements those earlier investigations with the focus on substorm effects in the magnetotail.

Compared to the previous empirical DM analysis of substorms (Stephens et al., 2019), this study is more focused on reconnection-related phenomena and processes at and beyond $\sim 20R_E$. Our approach provides rather a telescopic view of substorms, and in particular, it complements the recent MMS analysis of microscale non-MHD phenomena, such as EDR (Torbert et al., 2018), dipolarization fronts (Yao et al., 2017), and micro-instabilities (Le Contel et al., 2017).

The structure of the paper is as follows. In section 2, we overview the DM approach, the database extension, and the spatial expansion of the magnetic field. Reconstruction of the X-line associated with MMS observations of the 11 July 2017 EDR event is discussed in section 3. The reconstructed TGR features are discussed in section 4 on the example of the 2 February 2008 substorm. Violation of the isotropic force balance caused by long TCS as well as the opportunities to reconstruct from data interesting details of unsteady reconnection associated with substorm dipolarizations are discussed in section 5 on the example of four substorms on 13 February 2008. Finally, in section 6 on the example of the 5 January 2008 substorm, we describe a relatively rare case of the strong driving, with the solar wind electric field exceeding $\sim$ 5mV/m. Further error analysis of the DM method is presented in section 7. The results of this study are summarized and further discussed in section 8. For the sake of readability, most of validation results, as well as some details of the substorm morphology, which are interesting but not directly relevant to the main target of this study, non-MHD effects, are provided in the supporting information for this paper.

2. Methodology

2.1. Data-Mining Algorithm

The Earth's magnetosphere is a very large object, which is extremely sparsely sampled by in situ observations. At any moment, there are fewer than a dozen dedicated probes beyond low Earth orbit (LEO). Meanwhile, modeling and understanding of the global structure of the magnetospheric magnetic field, underlying currents, and pressure distributions, as well as their changes during major disturbances, storms, and substorms are fundamentally important to model and forecast space weather (Eastwood et al., 2017). Earlier attempts to attack these data paucity problem in empirical geomagnetic field modeling applied either

statistical (e.g., Tsyganenko & Sitnov, 2005, and refs. therein) or event-oriented (Kubyshkina et al., 1999) empirical models. Both approaches had to use relatively simple ad hoc parameterizations of the spatial distribution of magnetospheric currents. In the first case, simplification was suggested by the statistical nature of the model, where the whole database of historical records was used to derive a universal response of magnetospheric currents to the solar wind input. In the second approach, the number of the model's degrees of freedom was limited by the number of observations available at the moment of interest (not to exceed a dozen) to avoid overfitting. A new approach had been proposed a decade ago by Sitnov et al. (2008) as a trade-off solution between these two extremes. Its essence was to mine the data from a decade-long (1995–2005) multimission data archive and fit to them a new generation of high-resolution models (Tsyganenko & Sitnov, 2007), representing the field of key current systems by expansions into regular basis functions.

In the DM method employed, a relatively small number $K_{NN} \sim 10^4$ points, "most relevant to the event of interest," from the database of $K_{DB} \sim 10^6$ historical magnetometer records is used to reconstruct the magnetic field. This number is nevertheless much larger (by several orders in magnitude) than the number of data taken at the moment of interest of the modeled event. The NN subset is composed of the points in the database, which neighbor the event of interest in the "state space" of global parameters of the solar wind-magnetosphere system and hence they are termed the nearest neighbors (NN) (Cover & Hart, 1967; Vassiliadis, 2006). The state space is determined by the average low-latitude *Sym-H* index, reflecting magnetospheric activity during magnetic storms, its average time derivative, necessary to distinguish between storm main and recovery phases, and the average solar wind electric field parameter vB_z^{IMF} ($-v$ is the X-component of the solar wind and B_z^{IMF} is the Z-component of the interplanetary magnetic field (IMF)). An averaging time of several hours is used to eliminate the effects of substorms and concentrate on the storm-scale evolution of the magnetosphere.

The resulting DM-based empirical geomagnetic field reconstruction technology known as the TS07D model (Tsyganenko & Sitnov, 2007; Sitnov et al., 2008) was used to explore the spatial distribution and evolution of the ring current during storms driven by Coronal Mass Injections (CME) and Corotating Interaction Regions (CIR; Sitnov et al. (2008, 2010), as well as Steady Magnetospheric Convection (SMC) events (Stephens et al., 2013). Later, the increase in the size of the model's database and the number of degrees of freedom for equatorial currents allowed us to resolve more details of the storm-time current systems, including the eastward current and its closure paths with the main (westward) partial ring current forming a horse-shoe-like current structure (Stephens et al., 2016), as well as storm-time distributions of the plasma pressure (Sitnov et al., 2018). Similar improvement of the field-aligned current (FAC) system (Sitnov et al., 2017) revealed the spiral structure of the low-altitude FAC distributions, which can be independently reconstructed using LEO spacecraft observations (Iijima & Potemra, 1976).

Most recently, the DM approach has been extended to the description of substorms (Stephens et al., 2019). The DM binning space in this approach is determined by five functions $G_1 - G_5$ consisting of storm and substorm indices *Sym-H* and *AL*, their time derivatives, as well as the substorm-scale solar wind input parameter vB_s^{IMF} (here B_s^{IMF} is the southward component of the IMF: $B_s^{IMF} = -B_z^{IMF}$ if $B_z^{IMF} < 0$ and $B_s^{IMF} = 0$ otherwise):

$$G_1(t) = \langle Sym - H^* | \propto \int_{-\Pi_{st}/2}^{0} Sym - H^*(t+\tau)\cos(\pi\tau/\Pi_{st})d\tau \tag{1}$$

$$G_2(t) = D\langle Sym - H^* |/Dt \propto \int_{-\Pi_{st}/2}^{0} Sym - H^*(t+\tau)\sin(2\pi\tau/\Pi_{st})d\tau \tag{2}$$

$$G_3(t) = \langle AL | \propto \int_{-\Pi_{sst}/2}^{0} AL(t+\tau)\cos(\pi\tau/\Pi_{sst})d\tau \tag{3}$$

$$G_4(t) = D\langle AL|/Dt \propto \int_{-\Pi_{sst}/2}^{0} AL(t+\tau)\sin(2\pi\tau/\Pi_{sst})d\tau \tag{4}$$

$$G_5(t) = \langle vB_s^{IMF} | \propto \int_{0}^{\tau_\infty} vB_s^{IMF}(t-\tau_\infty+\tau)\exp[(\tau-\tau_\infty)/\tau_0]d\tau \tag{5}$$

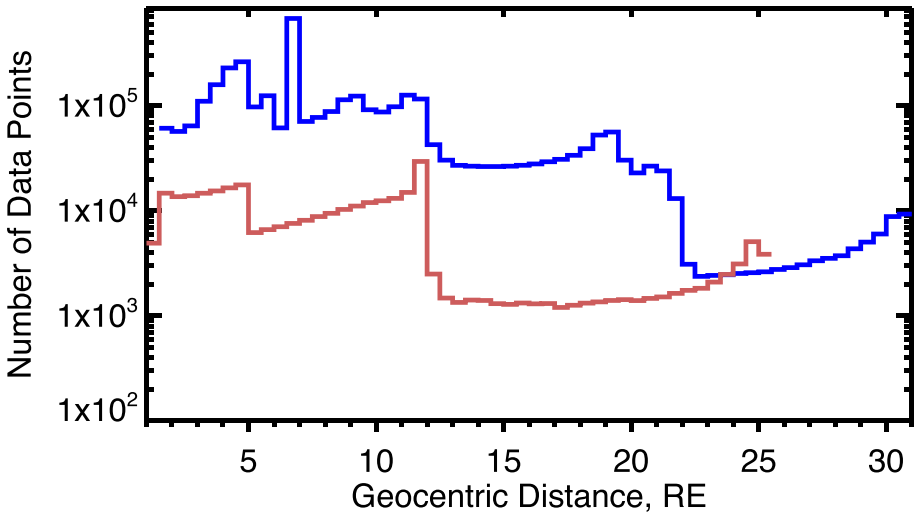

Figure 1. Radial distribution of the previous database (Stephens et al., 2019) shown by the blue line and the new 2016–2017 magnetospheric multiscale (MMS) data added to it in this study (red line).

Here $Sym-H^{*}=A\cdot Sym-H-B\cdot\sqrt{P_{dyn}}$ is the pressure-corrected $Sym-H$ index (Tsyganenko, 1996), P_{dyn} is the solar wind dynamic pressure (in nPa), and the values of A and B are taken to be 0.8 and 13.0, respectively. The functions G_1 and G_3 in (1) and (3) describe weighted moving averages of the indices $Sym-H$ and AL limited to their past values, while G_2 and G_4, defined by (2) and (4), describe the corresponding smoothed time derivatives. The asymmetric shape of the time averaging operators $\langle\ldots|$ reflects the fact that the window function only averages over past data (for more details on the filter functions, see Sitnov et al. (2012), and in particular their Figures 1 and 2). The averaging scaling parameters $\Pi_{st}=12\,\mathrm{hr}$ and $\Pi_{sst}=2\,\mathrm{hr}$ reflect the characteristic storm and substorm scales. Finally, the parameter G_5 defined by (5) describes the integral effect of the magnetic flux accumulation in the tail during growth phase due to the dayside reconnection. Its scale $\tau_0=0.5$ hr is selected based on observed values of a typical growth phase duration (Partamies et al., 2013). The selected upper integration limit in (5) $\tau_\infty=6\tau_0$ corresponds to six e-folding times. The main time constants used in our DM method are summarized in Table S1.

The NNs are determined as K_{NN} points $\mathbf{G}^{(i)}=[G_1(t_i),\ldots G_5(t_i)]$, $i=1,\ldots K_{NN}$, in the five-dimensional Euclidean space G_1-G_5 that are closest to the query point $\mathbf{G}^{(q)}=[G_1(t_q),\ldots G_5(t_q)]$ by the metric $R=\left[\sum_{j=1}^{5}\delta_j\left(G_j/\sigma_{G_j}\right)^2\right]^{1/2}$. Here σ_{G_j} is the standard deviation of the component G_j. The additional factors δ_j provide the opportunity to balance statistical weights of storm and substorm parameters as well as the solar wind input. Their default values are $\delta_j=1$.

2.2. Database Features

Following Stephens et al. (2019), the database used in this study includes spaceborne magnetometer records from 18 spacecrafts covering more than two decades of observations (1995–2016): IMP-8, Geotail, Polar, GOES-08, GOES-09, GOES-10, GOES-12, Cluster (4 probes), THEMIS (5 probes), and Van Allen Probes (2 probes). That set has 3,589,288 points with 15- or 5-min resolution (for details see Stephens et al., 2019). As one can see from Figure 1 (blue line), the corresponding distribution of data drops rapidly beyond $\sim 20R_E$. This may cause overfitting problems (see, for example validation tests in Figure 2e in Stephens et al., 2019) in that region, where the new X-lines are expected to form (e.g., Miyashita et al., 2000). To mitigate this problem in the present study, the database is extended by adding the 2016–2017 data from the MMS mission with a total number of 78,813 points. Thus, the total number of points in the database for this study is $K_{DB}=3,668,101$. As one can see from Figure 1, this practically doubles the data density in the region $22R_E<R<25R_E$.

2.3. Spatial Structure of the Magnetic Field Model

In addition to the new substorm binning parameters (3) and (5) in the DM procedure, the substorm version of TS07D (Stephens et al., 2019), which will be termed below, for the sake of brevity, SST19, has two important modifications of the magnetic field model structure. First, the magnetic field of equatorial currents is

presented as a sum of two similar expansions

$$\mathbf{B}^{(eq)}(\rho,\phi,z) = \mathbf{B}^{(eq)}(\rho,\phi,z;D) + \mathbf{B}^{(eq)}(\rho,\phi,z;D_{TCS}), \tag{6}$$

where (ρ,ϕ,z) are cylindrical coordinates in a system with the z axis normal to the equatorial plane. The two terms in the right hand side of (6) represent the magnetic field of thick and thin current sheets with the same structure determined by the approximate solution for the magnetic field of an arbitrary distribution of equatorial currents with the thickness $D^{'}$ (Tsyganenko & Sitnov, 2007):

$$\mathbf{B}^{(eq)}(\rho,\phi,z;D') = \sum_{n=1}^{N} a_{0n}^{(s)}\mathbf{B}_{0n}^{(s)} + \sum_{m=1}^{M}\sum_{n=1}^{N}\left(a_{mn}^{(o)}\mathbf{B}_{mn}^{(o)} + a_{mn}^{(e)}\mathbf{B}_{mn}^{(e)}\right) \tag{7}$$

but different thickness parameters D and D_{TCS} and therefore different resulting distributions in the equatorial plane. Here $\mathbf{B}_{\alpha\beta}^{(\gamma)}$ are the basis functions and $a_{\alpha\beta}^{(\gamma)}$ are their weights in the expansion. The solution (7) can be obtained by solving the Ampère's equation for the magnetic field of an infinitely thin CS ($D^{'}=0$) above and below the equatorial plane $z=0$ by separation of variables. As was shown by Tsyganenko and Sitnov (2007), the solution contains axially symmetric radial expansions (the first group of terms in (7) marked by the index (s)) , as well as even and odd in azimuthal angle ϕ groups marked by the indices (e) and (o), respectively.

The resulting solution for the vector potential of an infinitely thin CS contains factors like $\exp(-k|z|)$. Their regularization by the replacement of the function $|z|$ by the function $\zeta = \sqrt{z^2+D'^2}$ introduces the CS half-thickness $D^{'}$ and allows one to search different distributions of thick and thin current sheets. The resulting model of the tail current sheet resembles the TCS model of Pulkkinen et al. (1991), where a solution of the the Ampère's equation for a CS with a finite thickness was also used. However, the latter models assumed only a single-scale CS with one thickness parameter. That single-scale CS could vary in thickness depending on the position in the equatorial plane (x,y), but its variation was restricted by the predefined shape of the TCS region in that plane. In contrast, the model represented by (6) describes two-scale CSs that have a potential to reproduce the observed embedded and bifurcated TCSs (Asano et al., 2005, and refs. therein). To distinguish between thick CS and TCS, we impose the condition $D_{TCS} < D_{TCS}^{(\max)}$, where $D_{TCS}^{(\max)}$ is an intermediate CS thickness between TCS and thick CS (e.g., $1R_E$). Moreover, in contrast to Pulkkinen et al. (1991), the equatorial distributions of the current density in thick and thin CSs are not predefined in our model. Therefore the present model is more flexible as it can describe more complex CS configurations.

To give an example of the basis functions used in (7), we provide here the azimuthal component A_ϕ of the vector potential corresponding to the first group of basis functions $\mathbf{B}_{0n}^{(s)}$: $\left(A_\phi\right)_{0n}^{(s)} = J_1\left(k_n\rho\right)\exp\left(-k_n\sqrt{z^2+D'^2}\right)$, where J_1 is the Bessel function of the first order, $k_n = n/\rho_0$, and ρ_0 is the radial scale, corresponding to the largest mode in the radial expansion. While the parameters ρ_0, N, and M are fixed because they determine the adopted resolution of the expansions (7), other parameters, such as the weights $a_{\alpha\beta}^{(\gamma)}$ and the two-scale CS thickness parameters D and D_{TCS}, are determined from fitting the model to data. Thus, the spatial resolution of such an expansion is determined by the number of terms in (7) and can be increased to any desired level, commensurate with the data density. Note that each element in (7) is independently shielded (has its own subsystem of Chapman-Ferraro-type currents at the magnetopause).

SST19 also includes a flexible FAC system (Sitnov et al., 2017), necessary to reproduce the spiral FAC structure at low latitudes. Its importance was found in the first substorm reconstructions (Stephens et al., 2019), and it is likely explained by the important role played by the Harang reversal region (Harang, 1946) in the substorm reconfigurations of the magnetosphere (Zou et al., 2009). Each element of the FAC system is described as the magnetic field of two deformed conical surfaces corresponding to Region 1 (R1) and Region 2 (R2) FACs (Tsyganenko, 2002). The size of each system is an adjustable parameter, while their azimuthal distribution is controlled by the relative contributions of two groups of basis functions with odd and even symmetry due to factors $\sin(l\phi)$ and $\cos(l\phi)$, $(l=1,2,\ldots)$. The first group represents the main part of the FAC system, in which the dusk-side currents have the same magnitude but opposite direction to those at dawn, while the second group has an even distribution of currents with respect to the noon-midnight meridian plane, which allows one to model the azimuthal rotation of the FACs. In TS07D, the FAC system was described by the first and second harmonics $(l=1,2)$ with the odd $(\sin(l\phi))$ symmetry for R1 currents and the first harmonic $(l=1)$ with both odd and even and symmetry for R2 allowing its azimuthal rotation.

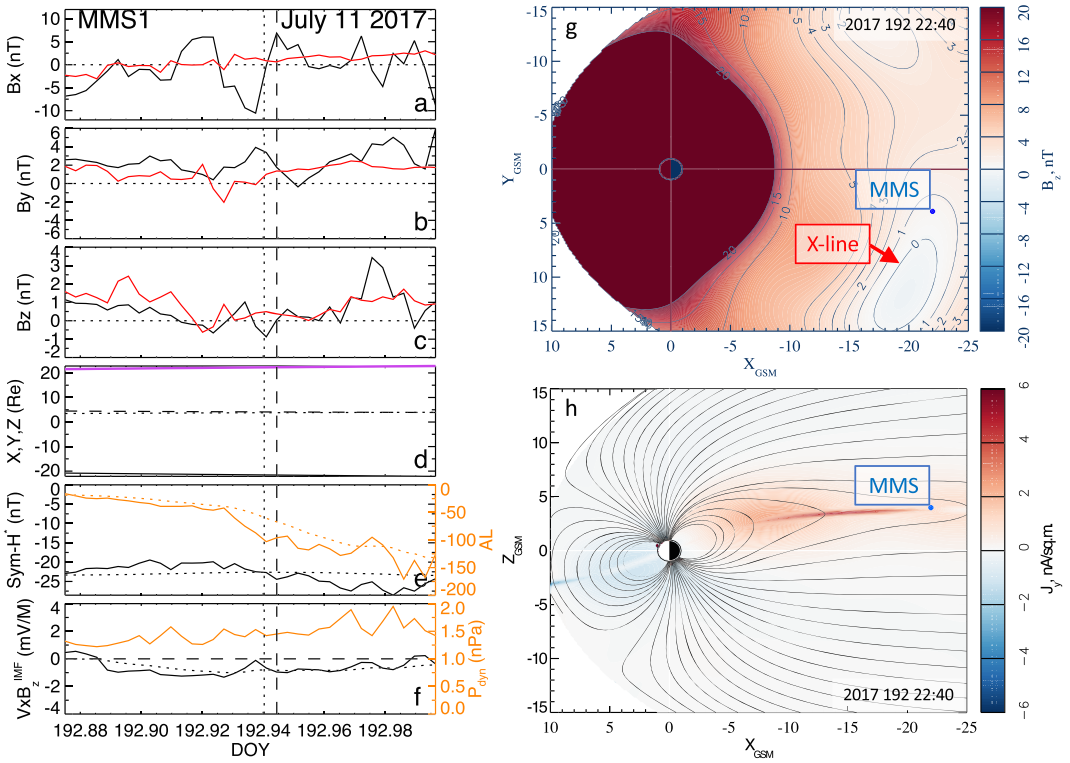

Figure 2. SST19 reconstruction of the 11 July 2017 EDR event (Torbert et al., 2018). (a–f) Validation results using 5-min MMS1 data. Panels from top to bottom show (a)–(c) observed (black lines) and reconstructed (red lines) values of the GSM magnetic field components, (d) the MMS ephemeris (X, Y, Z, and R components correspond to the black solid, dashed, dotted, and purple lines), (e) $Sym-H^*$ (black line) and AL (orange line) indices of storm and substorm activity, as well as (f) the solar wind electric field parameter vB_z^{IMF} (black line) and solar wind dynamic pressure P_{dyn} (orange line). Dotted lines in panels (e) and (f) show the smoothed values of indices and solar wind electric field corresponding to their DM input functions (1), (3), and (5). Vertical dotted and dashed lines mark the X-line crossings in high-resolution (22:34 UT) and 5-min (22:40 UT) data, respectively. (g) The distribution of the equatorial magnetic field B_z (using zero tilt angle) and (h) the Y-component of the current density with overplotted magnetic field lines in the noon-midnight meridional plane at 22:40 UT, corresponding to the vertical dashed line in panels (a - f). Magnetic field lines start from the ionosphere at 60° with 2° step in latitude. Blue dots mark the position of the magnetospheric multiscale (MMS) spacecraft. The X-line in panel (g) corresponds to the earthward part of the contour $B_z = 0$.

Sitnov et al. (2017) proposed to use modules similar to the original TS07D FAC basis functions shifted in latitude to fill the possible gap between R1 and R2 distributions. In this study, following Sitnov et al. (2017) and Stephens et al. (2019), we describe the FAC system using 16 basis functions with the first two Fourier harmonics ($l = 1, 2$) for R1 and R2, as well as their latitude-shifted clones.

An important distinctive feature of TS07D and SST19 as DM-based geomagnetic field reconstruction techniques is that given more data in the database and/or more dimensions in the description of the state of the magnetosphere (e.g., due to the substorm index AL and its time derivative), they may provide more details about the magnetosphere structure and evolution. This is a distinctive feature of *machine-learning algorithms* (e.g., Kubat, 2015). At the same time, for a given size of the database and given complexity of the model (i. e., the numbers of equatorial expansions (M, N) and FAC basic elements), there is an optimal range of K_{NN} values where the reconstruction is stable (no overfitting) and yet useful (that is, it resolves important storm or substorm spatial or temporal patterns). For the present database and the numbers of equatorial and FAC basis functions specified below, the range of NN numbers $K_{NN} = 16,000 - 32,000$ has been found to be optimal. Smaller K_{NN} values may cause overfitting, while larger values result in excessive statistical averaging and missing important details. As we show below, further optimization is rather difficult because of the very limited number of in situ observations for every event of interest and the dependence of validation results on the location (e.g., radial distance) of observations. In the following, to distinguish between the magnetic field models TS07D and SST19, on the one hand, and the whole set of data mining and fitting

procedures for storms and substorms, we will use below the terms STDM (Storm Time Data Mining) for the former and SSTDM (SubStorm Time Data Mining) for the latter.

3. Global Context of MMS Observations: 11 July 2017 EDR Event

To demonstrate the merits and limitations of the SSTDM reconstruction technique, we first consider the 11 July 2017 magnetotail reconnection event, which has been investigated at micro scales by Torbert et al. (2018) using MMS data. The X-line crossing at 22:34 UT is seen in their study as a change of the direction of the L-components of ion and electron bulk flow velocities, as well as the N-component of the magnetic field. The (LMN) coordinate system with L in the outflow direction, M along the X-line, and N normal to the current sheet was closely aligned with the GSM system (XYZ). Figure 2 shows validation results of SSTDM using 5-min MMS1 data for this event. The reconstruction is made with the method parameters (sections 2.1 and 2.3) $K_{NN} = 16,000$, $\rho_0 = 20R_E$, $(M, N) = (6, 8)$, $D_{TCS}^{(\max)} = 1R_E$, 16 FAC components and $N_{it} = 50$ iteration steps in adjusting the nonlinear parameters of the model magnetic field, such as D, D_{TCS}, hinging distance, and FAC scaling parameters (for more detail see; Stephens et al., 2019; Tsyganenko & Sitnov, 2007).

As is seen from Figure 2c, 5-min averaging causes a shift of the actual crossing time by 6 min to 22:40 UT. At the same time, the validation results in the B_z component turn out to be amazingly accurate, being within ~1nT of observations. The most significant deviations of up to ~10nT are seen in the B_x component. They are most likely caused by the CS flapping motions, which represent the CS eigenmodes. The latter may grow spontaneously (e.g., Sitnov et al., 2019) and hence cannot be reproduced by the DM method where similar substorm states of the magnetosphere are combined to obtain the generic features of the magnetosphere at the moment of interest.

The global distribution of the equatorial magnetic field at 22:40 UT provided in Figure 2g shows that, consistent with micro-scale MMS observations, the spacecraft was indeed close to an X-line—the earthward part of the contour $B_z = 0$. Figure 2h shows that it was also close to the neutral plane of the CS, at the tailward end of the TCS with the half-thickness $D_{TCS} \approx 0.2R_E$ (Figure 4e, orange line). The TCS was embedded into a much thicker CS with $D \approx 3R_E$ (Figure 4e, black line). Note that the location of X-lines at the tailward edge of a TCS was found earlier in the statistical analysis of Geotail data (Asano et al., 2004; Miyashita et al., 2009). The thickness of the EDR itself measured using MMS data (Figure 1i in Nakamura et al., 2019) $D_{EDR} \sim 50$ km $\approx 0.008R_E$ was much smaller than D_{TCS}. And the EDR was also very localized in the X-direction with $L_{xEDR} \sim 0.04R_E$ (Nakamura et al., 2019; Torbert et al., 2018). The SSTDM method cannot resolve these micro scales. It only helps reconstruct global and intermediate ($\sim D_{TCS}$) scales. Thus, it complements MMS studies.

To show the global 3-D configuration and topology of magnetic field lines for this event, we present in Figure 3 two sets of sample field lines at the moment 22:40 UT. In the first set (blue lines) tracing goes outwards from the near-Earth region with foot points being evenly distributed in latitude and longitude. In the second set (black lines), it starts from the $8R_E \times 8R_E$-size square located in in the equatorial plane, centered at $(-20R_E, 10R_E)$ with five grids in each dimension. In spite of the fact that the X-line is at the limit of the SSTDM resolution, the 3-D picture clearly shows the flux rope with the field lines winding up on the O-line. The X-line in this figure is seen as a white arc on the left of the rope, with the curvature opposite to that of the O-line. Since in this visualization we used zero tilt angle, the 2-D color-coded distribution of the equatorial magnetic field B_z is consistent with Figure 2g, where the X-line is marked by the red arrow.

More information about the global context of this event, the magnetic field, and current dynamics, compared to conventional substorms, can be gained from Figure 4. It describes the evolution of the SSTDM reconstruction parameters for ~ 1.5 hr around the EDR event in the format similar (but not identical) to Figures 6–8 in Stephens et al. (2019). This period was classified as a weak substorm (e.g., Nakamura et al., 2019). Following Stephens et al. (2019), we consider its growth phase starting from the first point with $B_z^{IMF} < 0$ in the 5-min cadence series (vertical red dashed line). The onset time 22:15 UT (vertical orange dashed line) is selected because of the strong change of the negative slope of the $AL(t)$. Note that this time is different here from the moment 22:33 UT when the westward electrojet commenced (Nakamura et al., 2019). The start of the recovery phase (23:40 UT, vertical blue dashed line) corresponds to the minimum of the AL index.

The comparison of Figure 4 with Figures 6–8 in Stephens et al. (2019), describing typical substorm evolution cases (see also other substorm examples below), shows that the 11 July 2017 substorm was rather unusual,

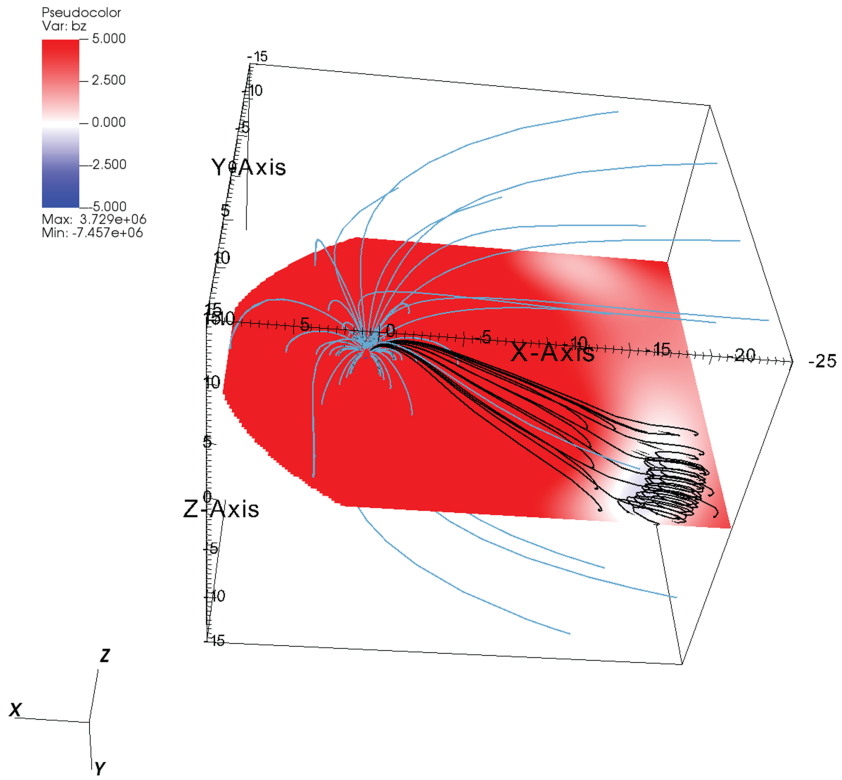

Figure 3. Sample field lines for the 11 July 2017 substorm reconstruction at the moment 22:40 UT. Here the zero tilt angle has been applied to make the 2-D color-coded distribution of the equatorial magnetic field B_z consistent Figure 2g (for visualization convenience, the magnetic field is saturated here at $|B_z| > 5$ nT). The blue lines are traced from the near-Earth region being equally spaced in the spherical coordinate system with six grids in latitude and 16 grids in longitude. The black lines are traced from a $8R_E \times 8R_E$-size square with five grids in each dimension in the equatorial plane centered at $(-20R_E, 10R_E)$. The starting points are marked by big dots.

even in contrast to conventional substorms of the similar strength in terms of the *AL* minimum (Figure 8 in Stephens et al., 2019). In particular, it did not provide any substantial dipolarization of the B_z field in the expansion phase (Figures 4g and 4i) or any substantial variations of the field-aligned currents (Figures 4c and 4d), thin and thick CS amplitudes (Figure 4f). This is consistent with relatively small reconnection electric field detected by MMS $E_M \sim 3$ mV/m (Genestreti et al., 2018; Torbert et al., 2018), which is by an order of magnitude smaller compared to the remote-sensed estimates for the reconnection electric field for the 10 August 2016 intense ($AL_{\min} \sim -1000$ nT) substorm (Nakamura et al., 2018). Its SSTDM analysis provided in Figure S1 shows clear signatures of thinning and dipolarization around 10:00 UT. In particular, the orange line in Figure S1f shows buildup and decay of the TCS amplitude, while Figures S1g and S1i show substantial variations of the equatorial magnetic field B_z. Thus, the SSTDM approach helps reconstruct a number of interesting features of the main MMS tail reconnection events.

4. 2 February 2008 Substorm: Magnetic Flux Redistribution

In the rest of this paper, we consider several substorms with *AL* minima ranging from −300 to −800nT and conventional signatures of stretching and dipolarization in growth and expansion phases, similar to those shown in Figure S1 that can be validated using multiple THEMIS probes. First, we consider the 2 February 2008 substorm with $AL_{\min} \sim -800$ nT. The results of validation of the SSTDM reconstructions for this substorm with different parameters using four THEMIS probes A, B, D, and E are provided in Figure S2. (Probe C data were not available for the period 2008-01-28/00:00UT to 2008-02-03/24:00UT, including this event, because of the cold reset issue (A. Runov, Private Comm.).) It is seen that the optimal reconstruction (red lines) with $(M, N) = (6, 8)$, $K_{NN} = 32,000$ and $N_{it} = 200$ reproduces dipolarizations observed by probes A and D located at $R \approx 10R_E$. It also reproduces fairly well variations of B_x and B_z components measured by the probe B at $R \approx 30R_E$, even though it was located at the edge of the main cloud of records in the

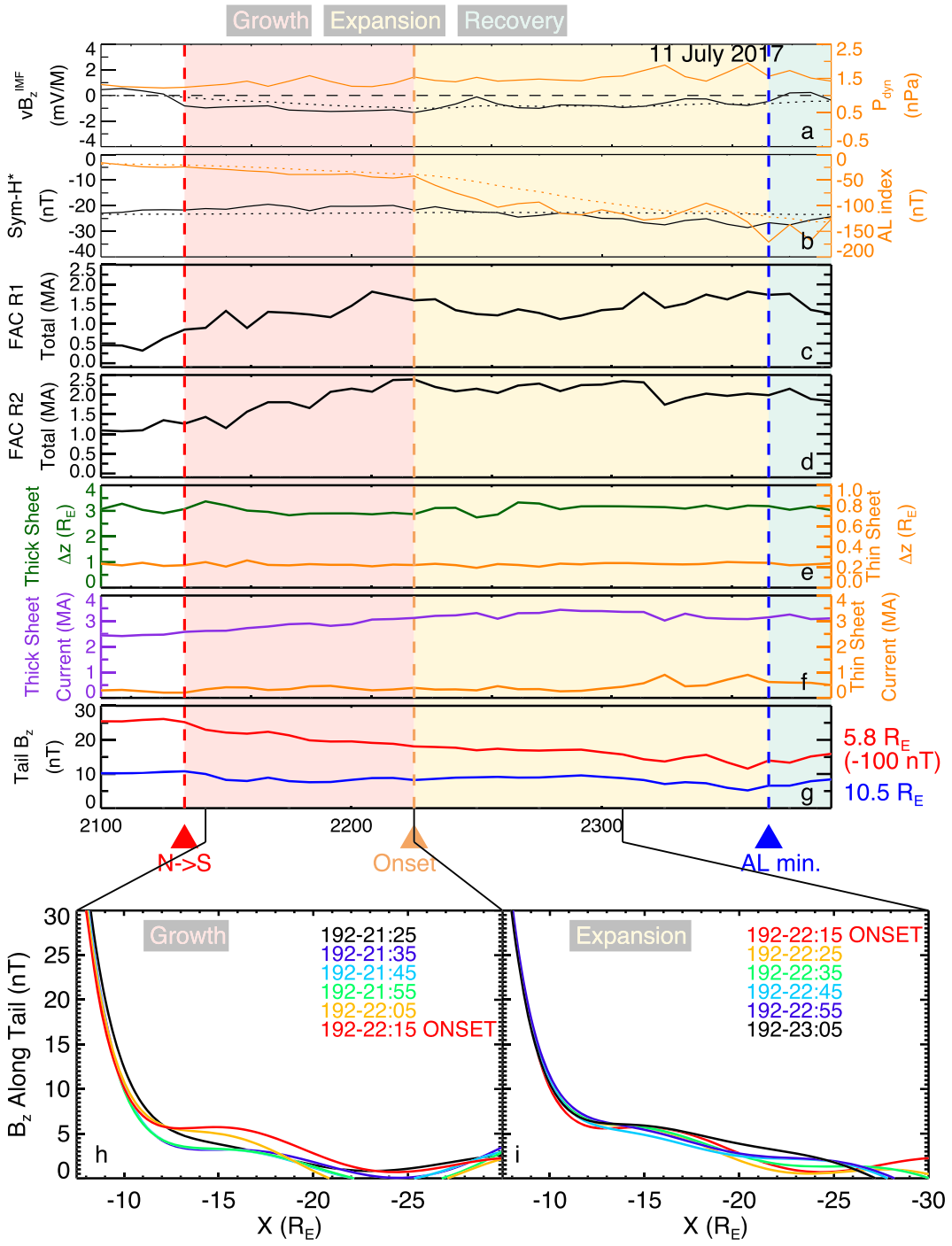

Figure 4. Analysis of the 11 July 2017 event. (a and b) Solar wind electric field vB_z^{IMF} and dynamic pressure P_{dyn}, as well as indices $Sym-H$ and AL (dotted lines show the corresponding smoothed values similar to Figures 2f and 2e). (c and d) The square root of the sum of the squared amplitude coefficients for the high and low-altitude parts of the field-aligned current (FAC) modules, respectively (labeled here as FAC R1 and FAC R2). (e) The equatorial current sheet (CS) half thickness parameters D (green) and D_{TCS} (orange). (f) The westward current from the thick CS module passing through the rectangle: $-16R_E \le X \le -6R_E$ and $-5R_E \le Z \le 5R_E$ (deep violet) and the westward current from the thin current sheet (TCS) module passing through the rectangle: $-16R_E \le X \le -6R_E$ and $-1R_E \le Z \le 1R_E$ (orange). (g) Total modeled B_z field sampled at $\mathbf{r} = (-5.8R_E, 0, 0)$ in red and $\mathbf{r} = (-10.5R_E, 0, 0)$ in blue. The red line has been shifted by subtracting 100 nT to place it in the same range as the blue line. (h and i) Total modeled B_z sampled along the line $(-30R_E \le X \le -7.5R_E)$ during the growth and expansion phases, respectively. The moment of time, when each B_z-profile was sampled, is specified by the corresponding colored text in the format "DOY-hour-minute".

database. This is seen particularly well when the optimal SSTDM reconstruction (red lines) is compared with the baseline storm-scale STDM reconstruction, which uses parameters similar to the nowcasting version (Sitnov et al., 2012) of the original TS07D model (Sitnov et al., 2008) shown by blue lines (the details of the parameters are provided in Figure S2 caption).

The dipolarization detected by the probe E and seen in Figure S2c at 33:54UT (black line) is also captured by the SSTDM. However, it has a substantial offset, reflecting most likely the limited in MLT and spontaneous nature of the CS thinning and stretching processes (Saito et al., 2011) and the subsequent dipolarization (e.g., Ohtani et al., 1991). Similar lack of sensitivity of the reconstruction is seen for the B_x magnetic field component measured by the inner probes A, D, and E. It can be similarly explained by the local nature of the CS thinning. At the same time, the comparison of optimal reconstructions with its modification (orange lines) using the smaller number of NNs $K_{NN} = 4,000$ and more radial basis functions $(M, N) = (6, 20)$ reveals sensitivity of the model to B_x variations (this set of the SSTDM parameters is not used further for the magnetic field reconstruction because of the overfitting issues discussed in sections 2.2 and 2.3). This suggests that the thinning process may also be spontaneous and independent of the solar wind loading as suggested, for instance, by Saito et al. (2011). Note that, as is shown below, the evolution of the lobe field during this and other storms has clear signatures of the tail thinning and dipolarization, but they only appear after the integration over a substantial tail region ($10R_E$ in both X and Z directions, as is specified in the Figure 4 caption).

The analysis of this substorm shown in Figures 5 and 6 reveals an interesting process in its early growth phase (Figures 5h and 5i), which is different from the late growth phase evolution (Figure 6) but is similar to magnetotail plasma instabilities discussed recently in PIC and MHD simulation studies of magnetotail equilibria. Figure 5h shows that at 11:45 UT the equatorial B_z distribution has a hump at $x \approx -22.5R_E$, which transforms later (during the transition from the phase "Growth 1" to "Growth 2") into another hump located at $x \approx -14R_E$. As was shown earlier in PIC (Bessho & Bhattacharjee, 2014; Pritchett, 2015; Sitnov et al., 2013) and local MHD (Birn et al., 2018; Merkin et al., 2015) simulations, the presence of a tailward gradient of the B_z field on the earthward slope of the hump may cause spontaneous redistribution of the magnetic flux. In the kinetic (PIC) case, this instability resembles the long-sought ion tearing instability, and it indeed tears the magnetic field lines in the process (Pritchett, 2015), which was termed "flux starvation" (Sitnov et al., 2017) and is marked in Figure 5i. However, since initially it develops as an ideal MHD instability and it releases the magnetic flux accumulated in the tail to be transported closer to the Earth, it was termed by Merkin and Sitnov (2016) the Magnetic Flux Release Instability (MFRI).

The magnetic flux redistribution later in the growth phase, which is shown in Figure 6i, resembles the regimes discussed before, as is seen, for example, from Figure S1i, as well as Figures 6 and 7 in (Stephens et al., 2019). The role of MFRI in this late growth phase process is less clear, because the tail dynamics must already be strongly affected by the formation of the new X-line tailward of the new B_z hump.

These TGR features are consistent with the results of statistical visualization (Machida et al., 2009; Wang et al., 2004) and remote-sensing (Sergeev et al., 2018) of the substorm growth phase, although they reveal a more complex picture that is difficult to draw using either statistical or case studies. Note that this picture does not contradict other studies (Ohtani & Motoba, 2017; Petrukovich et al., 2013; Yue et al., 2015) where TGR signatures were less conclusive. In particular, Petrukovich et al. (2013) reported several TGR events, which were interpreted as SMC regimes because of relatively large B_z values exceeding ~ 5 nT. However, that result is consistent with the "secondary" TGR shown in Figure 6h, which is preceded in our case by the "primary" TGR farther in the tail (Figure 5h). Yue et al. (2015), using another machine-learning method, the so-called Supporting Vector Regression Machine investigated the evolution of the $B_z(x)$ distributions along the tail as a function of a special loading parameter PCPAE, a linear combination of the time integrated cross polar cap potential drop and the auroral index *AE*. PCPAE was interpreted as an energy loading index considering both the loading from the solar wind and the effect from the previous substorm. They have found (see their Figure 4) the progressive reduction of the B_z field and its earthward gradient with the increase of the PCPAE values. One cannot rule out that the largest possible values of that loading parameter, reflecting the state of the magnetosphere in the late substorm growth phase and having TGR features, had not been reached in that study. Most recently, Ohtani and Motoba (2017) investigated the evolution of the equatorial B_z field and its gradient along the tail in the transition region $-12R_E < x < -9R_E$ using the multi-probe analysis of THEMIS data. They have found that the B_z gradient is directed predominantly earthward,

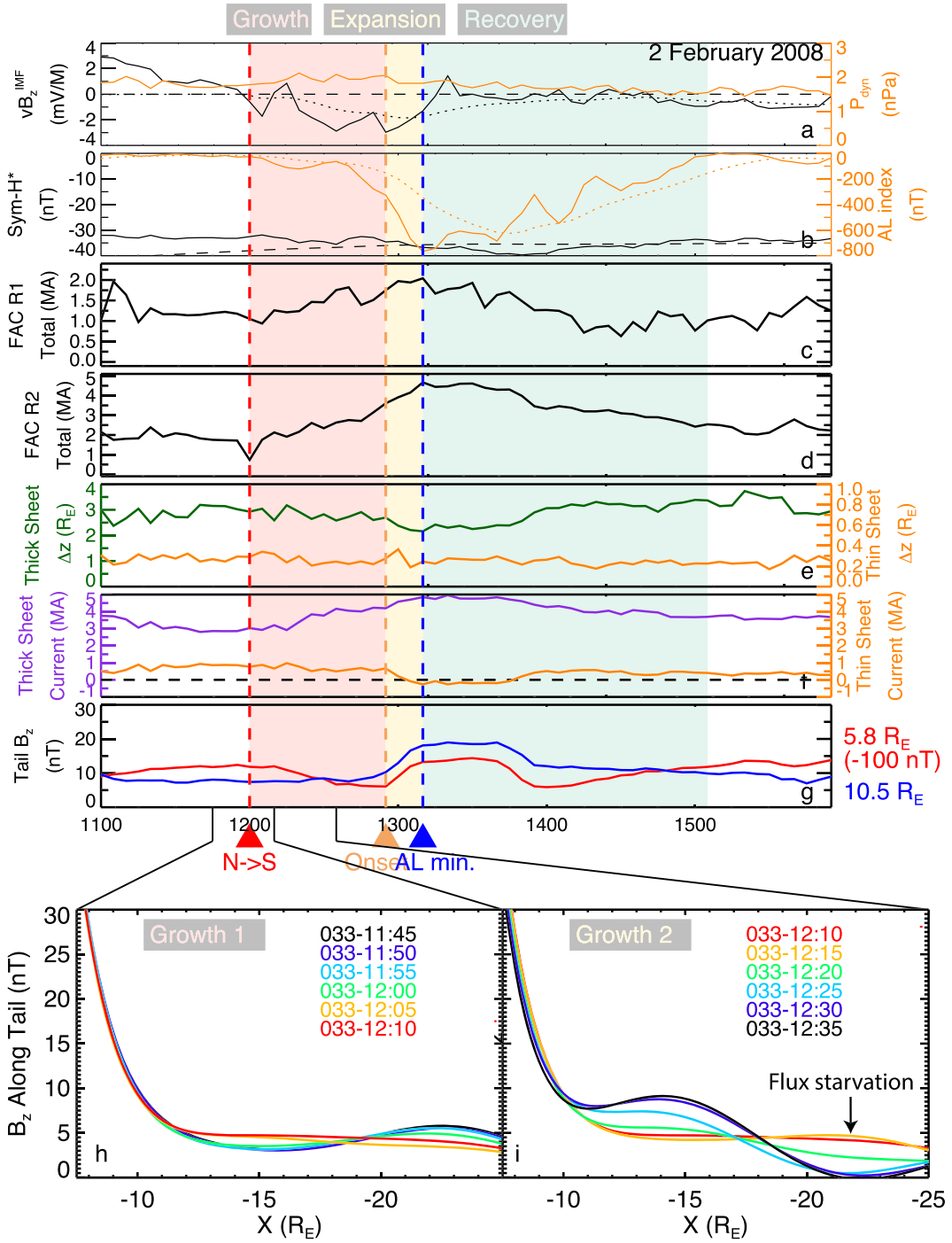

Figure 5. Analysis of the 2 February 2008 substorm in the format similar to Figure 4. Panels (k and i) show the evolution of the B_z field in early growth phase similar to the Magnetic Flux Release Instability (MFRI) process.

although in the growth phase the B_z field may become extremely weak ($\leq$ 2 nT). That result is also consistent with (Stephens et al., 2019) and the present study, where the TGRs are found beyond $\approx 11R_E$, with the only exception of a very strong driving case considered in section 6.

The orange line in Figure 5e shows that the TCS thickness during the event varies in the range $D_{TCS} = 0.2-0.3R_E$ whereas its amplitude, according to Figure 5f, rapidly drops after the substorm onset at 12:55 UT. At the same time, the thickness of the CS containing the TCS remains in the range $D = 2-3.5R_E$. Note that the amplitude of this thick CS is defined here differently than in (Stephens et al., 2019), where it reflected

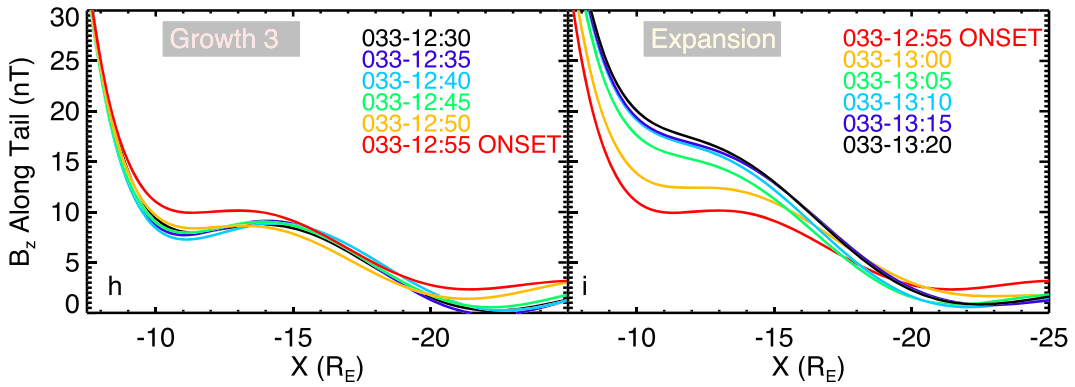

Figure 6. Extension of the analysis of the 2 February 2008 shown Figure 5. Panels (k and i) now show the evolution of the B_z field in the later growth and expansion phases.

a radial distance range closer to the Earth. Now it reflects the thick CS amplitude within the same distance along the tail $-16R_E \leq X \leq -6R_E$ as for the TCS. And due to integration in the z-direction over the interval $-5R_E \leq Z \leq 5R_E$ it reflects rather the evolution of the lobe field in the tail. Its buildup and decay during the substorm shown by the deep violet line in Figure 5f is more gradual, compared to TCS, and it is similar to the evolution of the lobe magnetic flux (e.g., Angelopoulos et al., 2013)

Global distributions of the equatorial magnetic field B_z and electric current are provided in Figures 7, S3, and S4. Panels (a)–(c) in these figures describe the field and current evolution during the MFRI process identified in Figures 5h and 5i. They show in particular that the initial region of the B_z minimum at $x \sim$

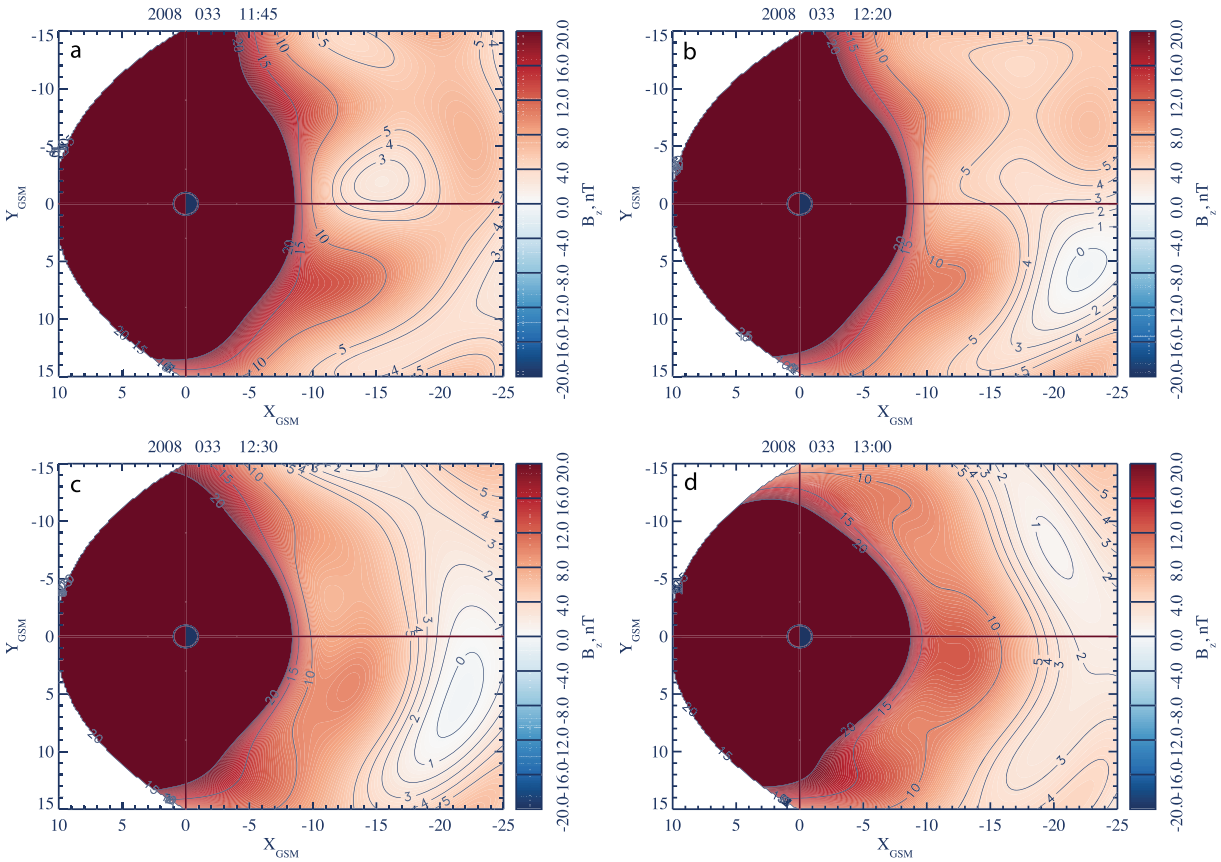

Figure 7. Distributions of the equatorial magnetic field B_z (using zero tilt angle) for the 2 February 2008 substorm in the format similar to Figure 2g: (a-c) Evolution of B_z during the Magnetic Flux Release Instability (MFRI) process and (d) at the beginning of the expansion phase.

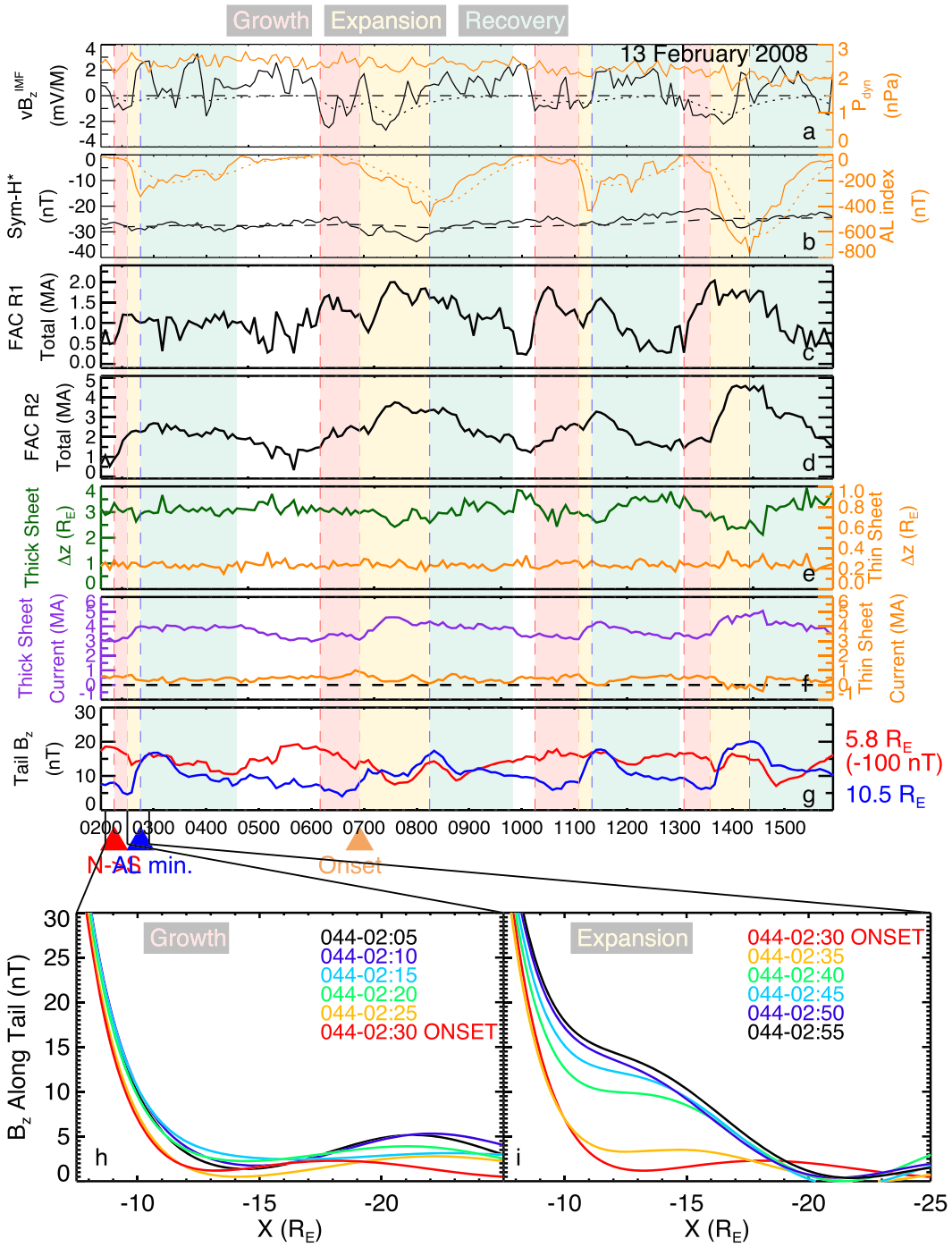

Figure 8. Analysis of the first event in the 13 February 2008 series of substorms in the format similar to Figure 4. Panels (h and i) now show the Magnetic Flux Release Instability (MFRI)-type evolution of the B_z magnetic field in the growth phase just prior to the substorm onset.

$-15R_E$ (Figure 7a), the subsequent partial dipolarization and the plasmoid formation enabled by the MFRI (Figures 7b and 7c) are limited to a few R_E in the dawn-dusk (Y) direction. This localization may explain the interchange stability of the initial B_z hump configuration. The localized in space and transient in time nature of the MFRI process, as well as its location further in the tail, beyond the quasi-dipolar region where the main substorm dipolarization takes place (Figure 6i) also suggest that it describes here the pseudobreakup mode of the tail activity (Koskinen et al., 1993; Ohtani et al., 2002, and refs. therein).

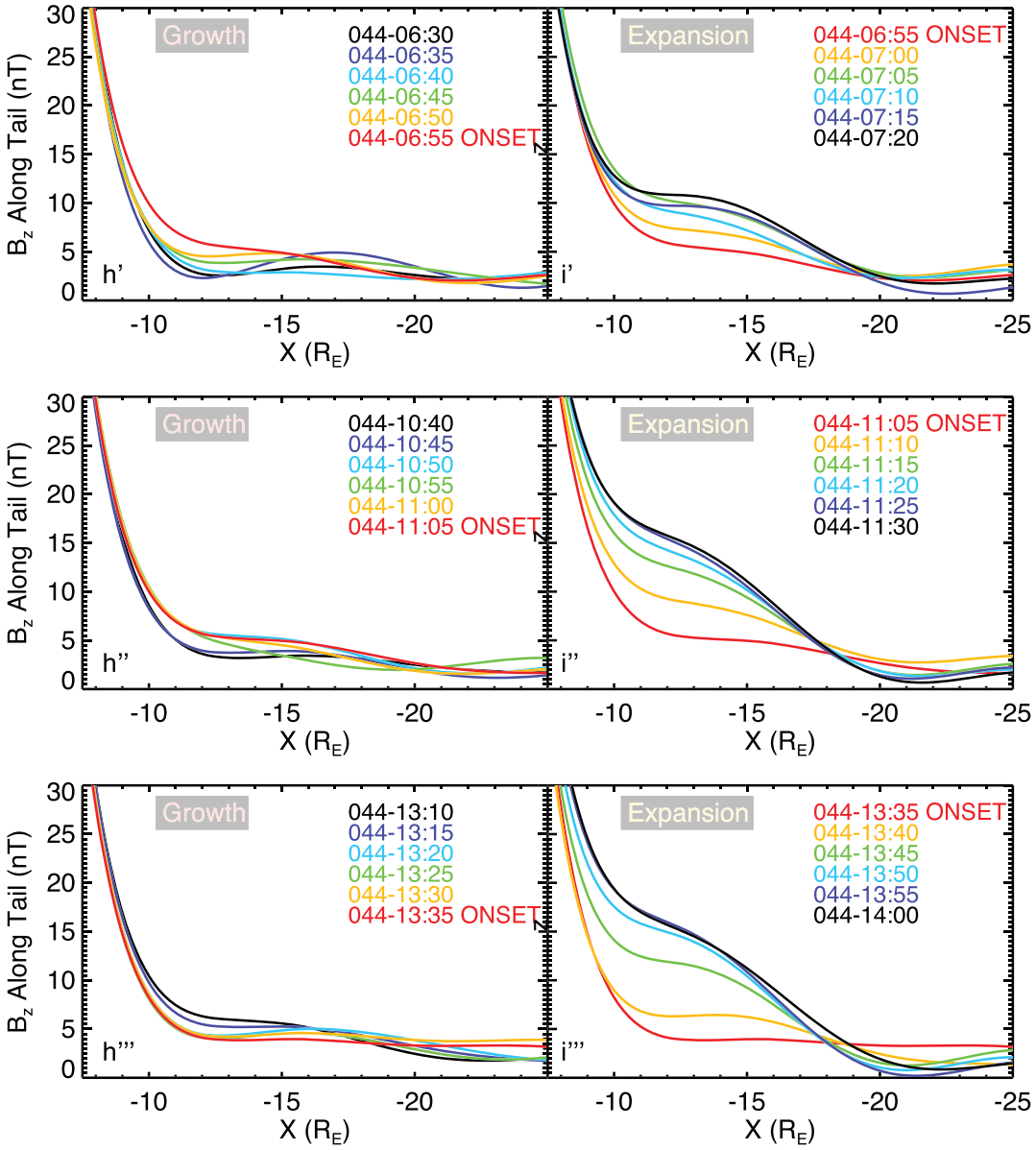

Figure 9. The evolution of the B_z magnetic field profile along the tail around the onset time for events 2–4 in the the 13 February 2008 series of substorms.

Finally, note that, according to Figure 5d, the amplitude of low-altitude field-aligned currents, described by the parameter FAC R2, persistently increases from the beginning of the growth phase to the end of the expansion phase in this substorm. At the same time, because of the spiral structure of FAC system, this growth is not limited to R2-sense currents, and as is seen from Figure S5, the FAC evolution is more complex. It includes an increase and equatorward expansion of both R2 and R1 currents with the formation of a clear spiral structure (Koskinen & Pulkkinen, 1995), associated with the Harang discontinuity (Harang, 1946), and the subsequent contraction of the FAC pattern in the recovery phase. This picture is consistent with the results of direct investigation of the low-altitude FAC current density using the magnetic field data from the Active Magnetosphere and Planetary Electrodynamics Response Experiment (AMPERE; Anderson et al., 2018, and refs. therein).

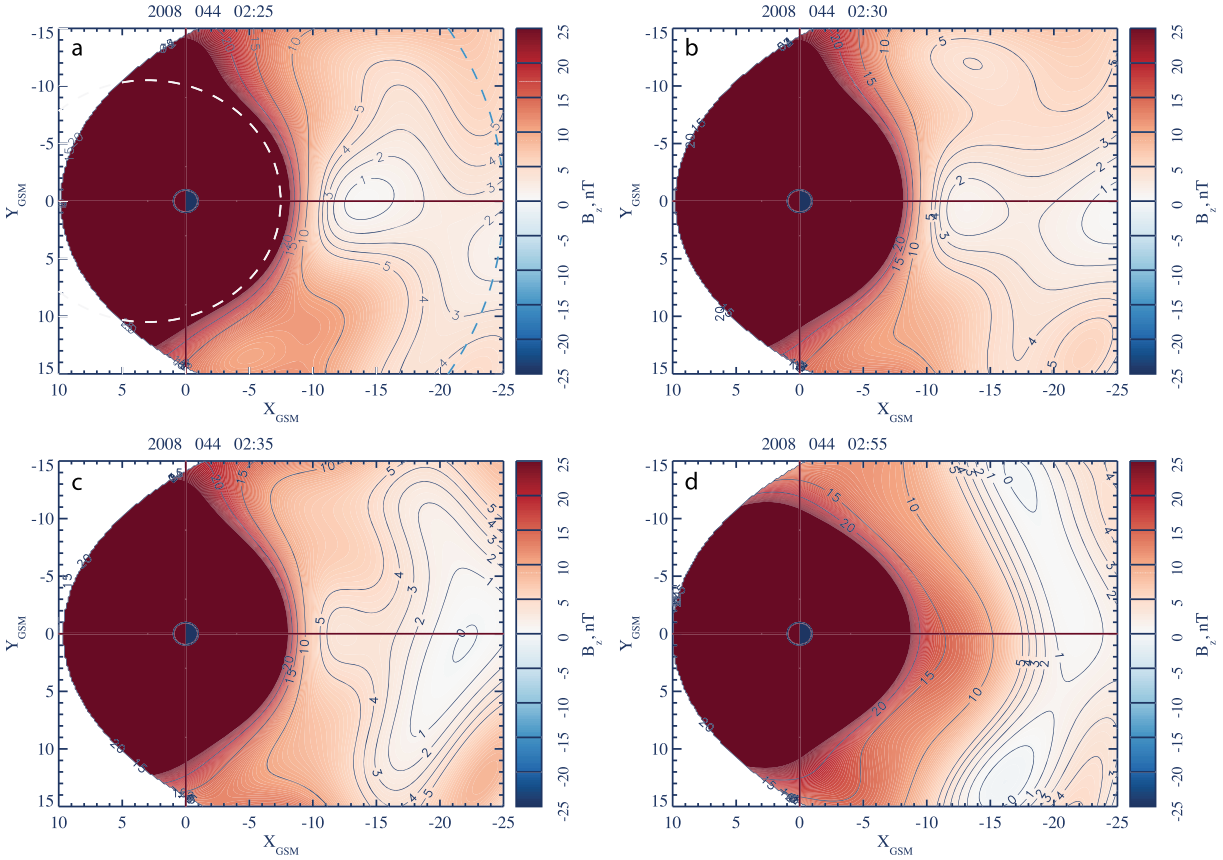

Figure 10. Distributions of the equatorial magnetic field B_z (using zero tilt angle) around the substorm onset for the first event in the 13 February 2008 series of substorms in the format similar to Figure 2g. Dashed white and blue arcs in panel (a) show sample integration paths, which are used below to evaluate the closed magnetic flux evolution presented in Figure 14.

5. February 13, 2008 Substorms: Unsteady Reconnection and Non-MHD TCSs

Further insight into the morphology and dynamics of substorm currents is provided by the analysis of four events on 13 February 2008. The SSTDM validation results for these events are presented in Figures S6 and S7. They show that the reconstruction of the magnetosphere captures the main details of the tail stretching and dipolarization from geosynchronous orbit to $\sim 30R_E$ down tail.

The analysis of these events in Figures 8 and 9 reveals characteristic features already discussed in (Stephens et al., 2019) and earlier in this paper, namely, the TCS amplitude buildup and decay in growth and expansion phases, respectively (orange line in Figure 8f), B_z reduction and dipolarization seen in Figures 8g–8i and 9. Moreover, Figures 8h and 8i suggest that the MFRI-like redistribution of the magnetic flux, similar to the pseudobreakup discussed in the previous section, now takes place right before the substorm onset. The equatorial magnetic field distributions for the first of these substorms provided in Figure 10 show that the same local in MLT B_z minimum (Figure 10a) is now followed by the formation of a wide chain of flux ropes (Figure 10d). Another distinction is the buildup of a wide and long TCS around the onset time (02:30 UT) seen in the equatorial current distributions (Figures 11b, 11c, and 12c) and the decay of that TCS in the expansion phase (Figure 11d). It is noteworthy that the near-Earth magnetic field dipolarization is accomplished as quickly as in 5 min (the highest time resolution of the present reconstruction technique) as is seen from the comparison of yellow and green lines in Figure 8i.

Interesting details of the first substorm in the 13 February 2008 series are provided in Figure 13. It presents a color-coded distribution of the dusk component of the current density and field lines drawn by solid lines at the end of the expansion phase of this substorm (02:55 UT). This configuration is compared with the similar magnetic field line pattern at the substorm onset (02:30 UT) drawn by dashed lines. The comparison reveals several striking features. First, it shows that the magnetic field configuration at high and low latitudes (see

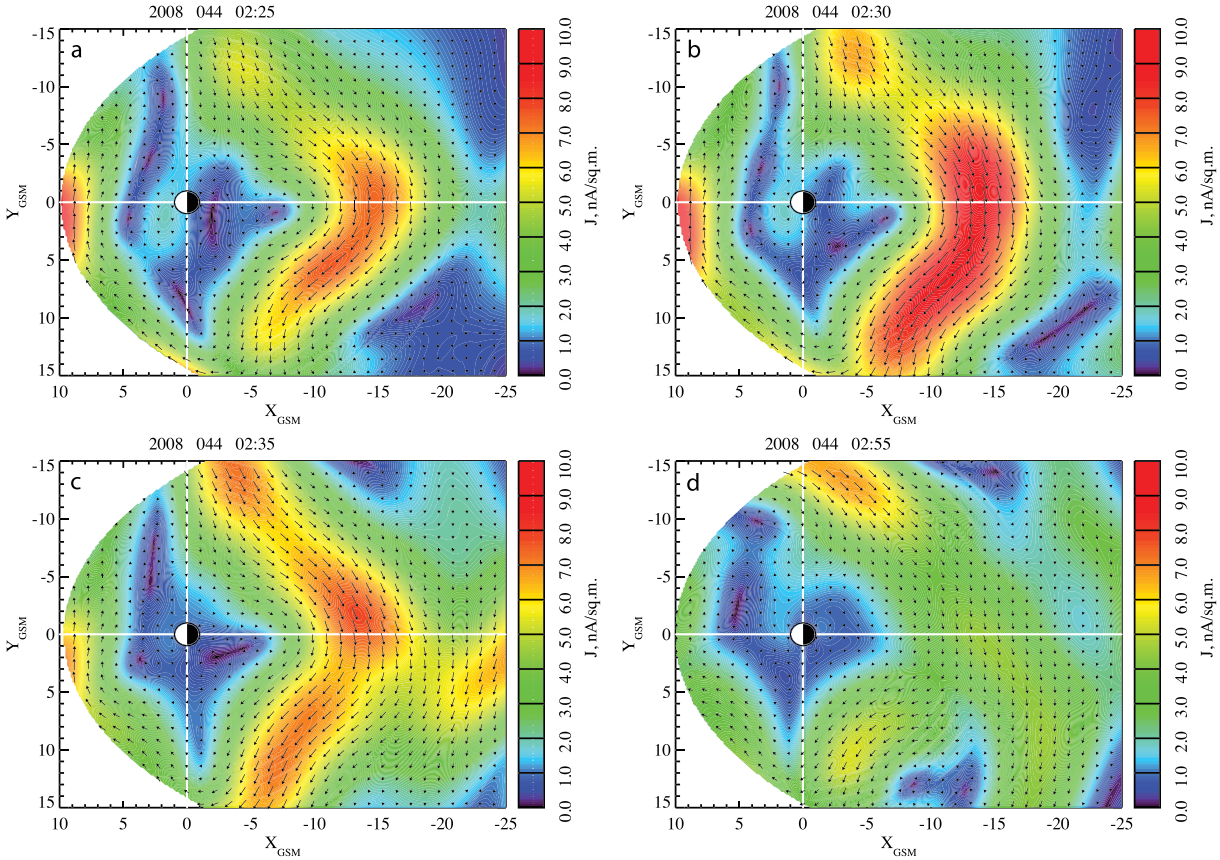

Figure 11. Equatorial current distributions (using zero tilt angle) for the moments of the 13 February 2008 substorm shown in Figure 10. The arrows are vectors of the equatorial current density whose absolute value is color coded.

the samples marked by green circles) exhibits almost no changes. Note that the small magnetic field perturbation at low latitudes, close to geosynchronous orbit, may be explained by the relatively short duration and small strength of this substrom, with $AL_{\min} \sim -300$ nT. Substantial perturbations of the equatorial B_z magnetic field inside geosynchronous orbit are seen for stronger substorms, such as the fourth event in the same group (Figure 8g, 13:30–14:00 UT), the 10 August 2016 event (Figure S1g) and the events considered in (Stephens et al., 2019, Figures 6 and 7).

At the same time, strong dipolarization is seen in the closed field line region, where blue circles show solid and dashed lines with similar low-altitude foot points, and their apex displacement is shown by the blue arrow. Finally, red circles and arrows show the transformation of open field lines to closed field lines that is the lobe field reconnection conjectured earlier in many works based on local in situ observations (e.g., Baker et al., 1996; Hones, 1984).

Judging by the displacement of the lobe field lines with similar near-Earth foot points (the region $x \approx -25R_E$ in Figure 13), during this substorm one can expect the poleward shift of the open-closed field line boundary on the midnight meridian by 2°–4°. This is consistent with the superposed epoch analysis of the open/closed boundary dynamics inferred from IMAGE observations (Milan et al., 2009, Figure 5).

Further analysis of the lobe field line displacement shows that the lobe reconnection proceeds rather slowly: $\sim 3R_E$ in 25 min or $\sim$ 12 km/s (note, however, that the magnetic field line picture variations do not reflect steady magnetospheric convection effects). This value is two orders in magnitude smaller compared to the characteristic Alfvén velocity in the magnetotail $v_A \sim 1,000$ km/s (based on the lobe field estimate ~ 40 nT and the plasma sheet density $\sim 0.5\,\mathrm{cm}^{-3}$), and in particular, it is smaller than characteristic values $\sim 0.1v_A$ obtained in kinetic simulations of collisionless magnetic reconnection (Birn et al., 2001; Shay et al., 1999). At the same time, it is surprisingly consistent with resistive MHD estimates and simulations of the reconnection rate, taking into account the effect of secondary island formation (Cassak et al., 2017, and refs. therein).

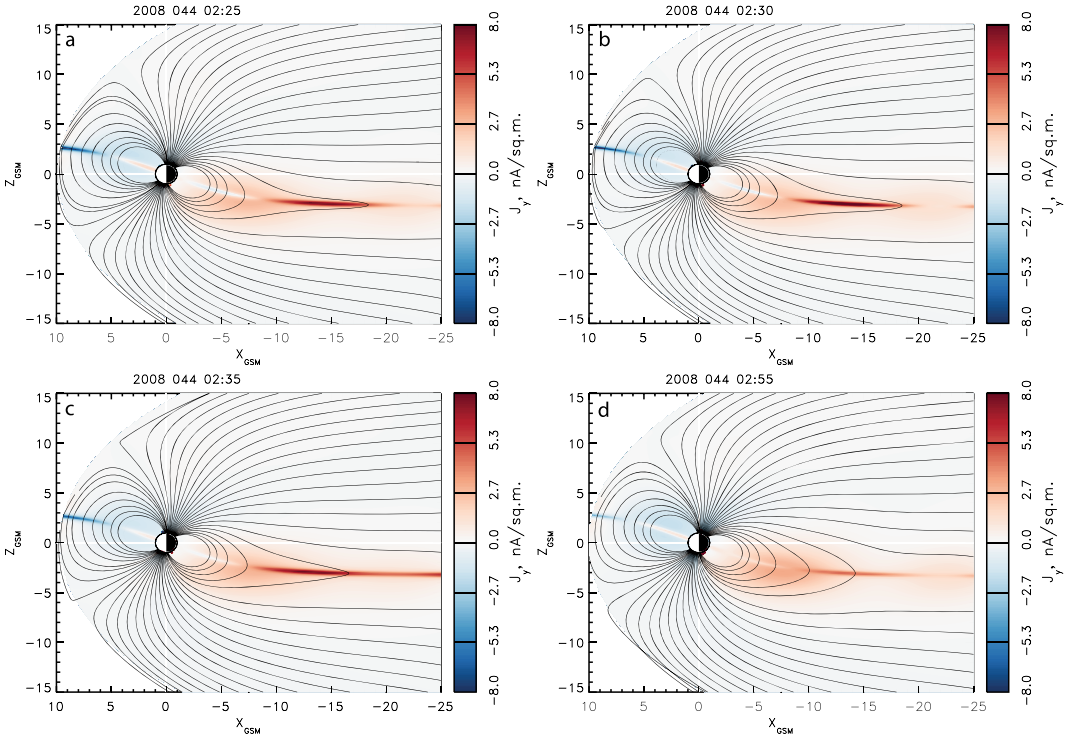

Figure 12. Distributions of the Y-component of the current density with overplotted magnetic field lines in the noon-midnight meridional plane for the moments of the 13 February 2008 substorm shown in Figure 10.

The effective reconnection electric field, $E \sim 0.5$ mV/m, associated with the magnetic flux redistribution shown in Figure 13, is substantially smaller, compared to local MMS observations of the electric field in the EDR discussed in section 3. This discrepancy can be explained by the nonsteady regime of reconnection, which is clearly seen from the magnetic field reconfiguration in Figure 13. As a result, in contrast to idealized 2D steady-state regimes of reconnection, when the electric field is constant in the meridional plane due to the Faraday's law ($\partial E_y/\partial x = -\partial B_z/\partial t$ and $\partial E_y/\partial z = \partial B_x/\partial t$), in a more realistic case of global magnetic field reconfiguration shown in Figure 13, this is definitely not the case. Inhomogeneous electric field distributions have been reported in a number of PIC simulations of unsteady magnetotail reconnection (e.g., Sitnov & Swisdak, 2011).

Relatively small values of a lobe reconnection rate also raise the issue of the explanation of the fast near-Earth dipolarization seen in validation plots (Figures S6 and S7) and in the reconstructed dipolarization signatures at 10.5 and 5.8R_E (Figure 8g). Its possible resolution is seen from Figure 14. It shows analogs of Figures 8h, 8i, and 9, but instead of the distribution of the equatorial B_z profiles, it now shows the line integral $Int(B_z) = \int B_z ds$ over arcs similar to dashed white and blue arcs in Figure 10a from the dusk to dawn magnetopause boundaries (the arc center is shifted by 3 R_E sunward relative to the Earth to avoid integration over whole circles within the magnetopause). The area under these curves is now magnetic flux, and thus the evolution of these curves describes the evolution of magnetic flux (rather than just the B_z field) in the closed field line region. Note that in the right panels ($i - i'''$), the increase in flux after onset in the region $10-17R_E$ is roughly equivalent to the decrease in flux at $17-25R_E$. This strongly suggests that the main part of the near-Earth dipolarization for all four substorms is provided by the redistribution, rather than an overall increase, of magnetic flux in the closed field line region.

These findings by no means rule out magnetic reconnection as the mechanism of substorm dipolarizations. To the contrary, they expose the fundamental physics of spontaneous magnetic reconnection, whose main free energy source, according to Galeev (1984), is the mutual attraction of parallel current filaments of the CS. Galeev (1984) noticed that in view of that physical mechanism, one can expect that the tearing instability in the tail current sheet with the finite B_z may represent spontaneous generation of stretched and dipolarized regions (termed in his seminal work as “compression” and “rarefaction” areas). That original

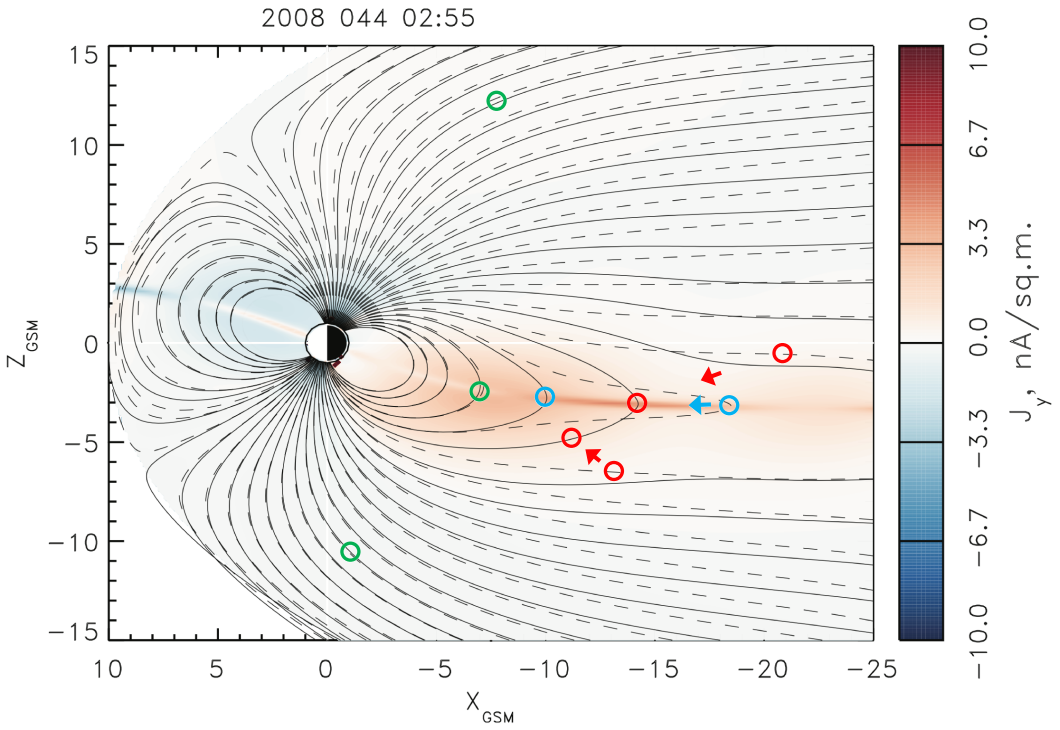

Figure 13. Details of the magnetic field reconfiguration obtained from the comparison of the late expansion phase in the first event in the 13 February 2008 substorm series (02:55UT), corresponding to Figure 12d, with the field line picture from the onset moment for that substorm (02:30UT, Figure 12b) shown by dashed lines. Blue circles and arrows mark the magnetic field redistribution in the closed field line region (note similar foot points for the corresponding solid and dashed field lines). Red circles and arrows mark the transition from open to closed field line region, which likely indicates the lobe field reconnection. Green circles mark the regions at lower and higher latitudes relative to the onset region that reveal weak changes of the magnetic field configuration and suggest that the process in between is internal for the magnetotail and likely spontaneous.

conjecture has later been confirmed by PIC and MHD simulations of magnetotail equilibria with B_z humps (Bessho & Bhattacharjee, 2014; Birn et al., 2018; Merkin et al., 2015; Pritchett, 2015; Sitnov et al., 2013, 2014, 2017). Moreover, PIC simulations confirmed that the onset of fast dipolarization, including the spontaneous generation of fast earthward flows with the speed $\sim v_A$, may proceed very rapidly, consistent with observations, as long as the CS thickness is comparable to ρ_{0i}. Furthermore, it was shown that the spontaneous dipolarization process leads, on the one hand, to the formation of dipolarization fronts, one of the most ubiquitous transient processes in the tail (e.g., Sitnov et al., 2019, and refs. therein), and on the other hand, it naturally causes the formation of new X-lines due to the flux starvation mechanism (Pritchett, 2015). The subsequent lobe field line reconnection does not have to be very fast, because it only replenishes the magnetic flux, which has become redistributed in the closed field line region because of the MFRI dipolarization. This magnetic flux replenishing may take the time of the whole recovery phase and the next growth phase. The corresponding global X-line is likely located around $30R_E$ (Figure S8), but the fidelity of reconstructions in that region is limited by the rapid drop of the data density beyond $31R_E$.

Large aspect ratios of the TCS observed in SSTDM reconstructions discussed above (Figures 2h, S4, and 12) suggest that they may violate the balance between the magnetic field line tension and the isotropic plasma pressure gradient $\eta_{IFB} = (B_0/B_z)(L_z/L_x) \cong 1$ (Cowley, 1978; Rich et al., 1972). Earlier estimates of this parameter were limited by either local observations (Pulkkinen et al., 1998) or used variations of the B_z field along the tail as an estimate of its inhomogeneity scale (Artemyev et al., 2015). The latter may be particularly limited in view of the fact that $\eta_{IFB} \approx 1$ for isotropic equilibria even with a constant small B_z (Schindler, 1972). Our global reconstructions of the magnetosphere, including its tail region, provide an opportunity to quantitatively assess the parameter η_{IFB} over a large part of the tail from the transition region to $R \sim 25R_E$. In particular, Figure 15 shows distributions of the parameter $|B_x(z = 5R_E)|/B_z(z = 0) \approx B_0/B_z$ along the tail in the growth phases of all four 13 February 2008 substorms. Figure 16 shows the meridional current

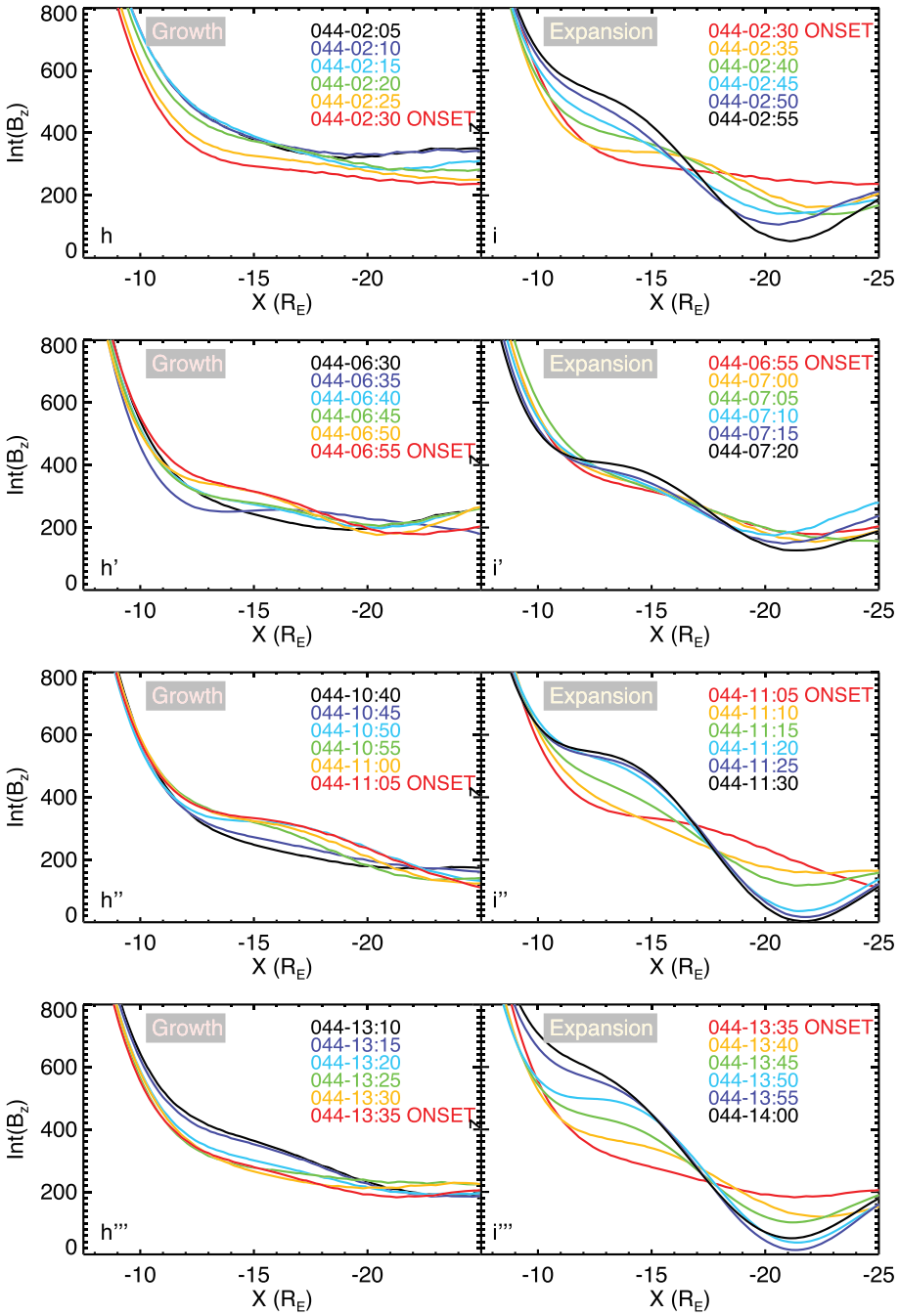

Figure 14. Analogs of Figures 8h, 8i, and 9, now showing the line integral $Int(B_z) = \int B_z ds$ over the arcs similar to dashed white and blue arcs in Figure 10a from dusk to dawn magnetopause boundaries (and expressed in units nT·R_E) as a function of the arc's most tailward value of x. The function $Int(B_z)$ better reflects the redistribution of the magnetic flux over the tail taking its width in the dawn-dusk direction into account.

distributions for selected moments in those growth phases when the parameter $|B_x(z = 5R_E)|/B_z(z = 0)$ does not exceed 10 (the blue line in Figure 15a and red lines in Figures 15b–15d, corresponding to onset moments). As follows from Figure 16, the TCS length L_x exceeds $10R_E$ (in the case shown in Figure 16d it even exceeds $15R_E$). Therefore, taking into account the TCS thickness evaluation provided in Figure 8e $D_{TCS} \approx 0.2R_E$, the TCS aspect ratio in all cases shown in Figure 16 exceeds 50. As a result, the isotropic force balance parameter $\eta_{IFB} \leq 1/5$.

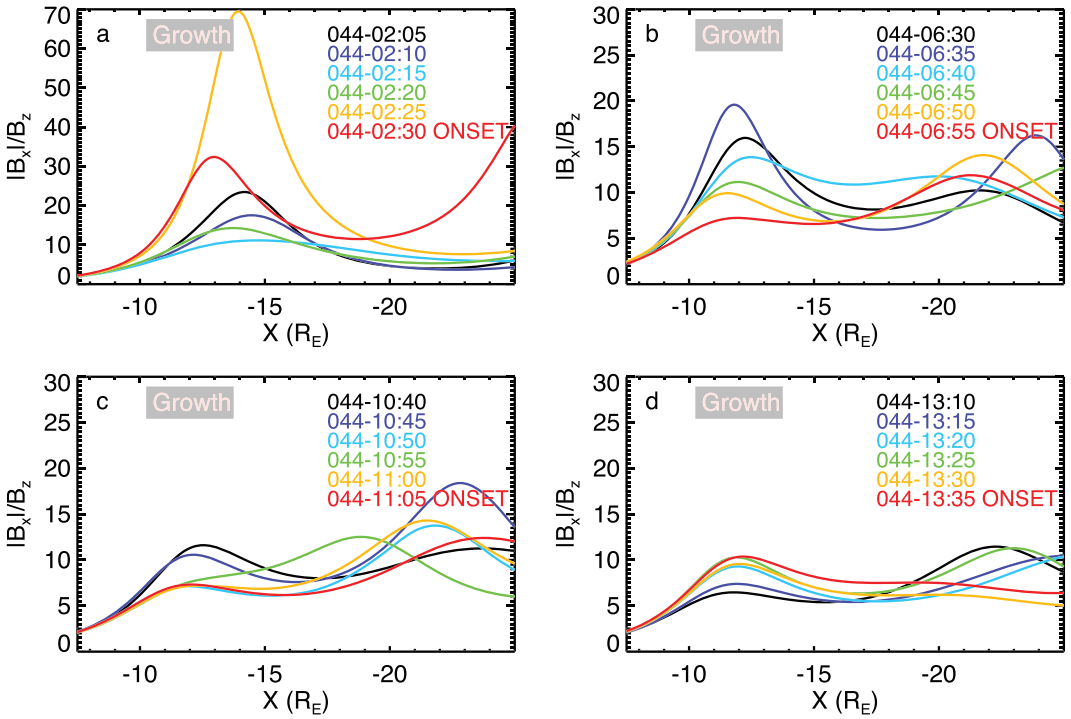

Figure 15. Distributions of the magnetic field stretching factor $|B_x(z = 5R_E)|/B_z(z = 0)$ along the tail in the growth phases of four 13 February 2008 substorms.

In fact, significant violations of the isotropic force balance are directly seen already from the meridional distributions of the magnetotail in the growth phase or just nonactive periods when the quasi-static relationship $\nabla p = \mathbf{j} \times \mathbf{B}$ suggests that the pressure gradient should be normal to the magnetic field. Assuming a 2-D approximation (e.g., Schindler, 2007), which should be valid sufficiently far from the dipole field region, this implies that the magnetic field lines should also be isocontours of the pressure and current density. However, Figures 2h, S4a–S4c, 12a–12c, and 16 reveal significant deviations of the magnetic field lines from the current density isocontours that can be grasped from its color coding.

This result suggests that prior to the substorm onset, balancing the magnetic field line tension in a TCS may require nonisotropic plasma populations. Such configurations can hardly be provided by conventional double adiabatic gyrotropic plasma models used in some recent global simulations (Meng et al., 2012) because they are shown to result in shorter tails with smaller aspect ratios, compared to isotropic models (Meng et al., 2013). It is more plausible that TCSs with larger than isotropic aspect ratios are provided by nongyrotropic effects of the figure-of-eight ion orbits (Speiser, 1965), as is demonstrated in equilibrium models of non-Grad-Shafranov TCSs (Sitnov & Merkin, 2016, and refs. therein) and suggested by global hybrid simulations (Lu et al., 2016).

From this result, it also follows that the analysis of reconnection onset mechanisms in the magnetotail cannot be limited to regimes with a tailward B_z gradient (Sitnov & Schindler, 2010) and demagnetization of electrons (Hesse & Schindler, 2001), but it should also include models with embedded non-Grad-Shafranov TCS equilibria (Zelenyi et al., 2008).

6. 5 January 2008 Substorm: Strong Solar Wind Driving Features

Finally we consider the first event of two 5 January 2008 substorms with a relatively strong driving (Figure 17). As is seen from Figure 17a, in this event the solar wind electric field exceeded $\sim$ 5mV/m and the dynamical pressure reached values of $\sim$ 7nPa. The results of the SST19 validation for these substorms provided in Figures S9 and S10 show that, while the major dipolarizations can be captured here using the SSTDM approach (see panels (c) in these figures), the persistently elevated B_z values, which last for several hours are very difficult to reproduce with the present method. Yet, the analysis of this event clearly shows the formation of a near-Earth X-line at $x \sim -15R_E$ (Figure 17h) and its subsequent tailward

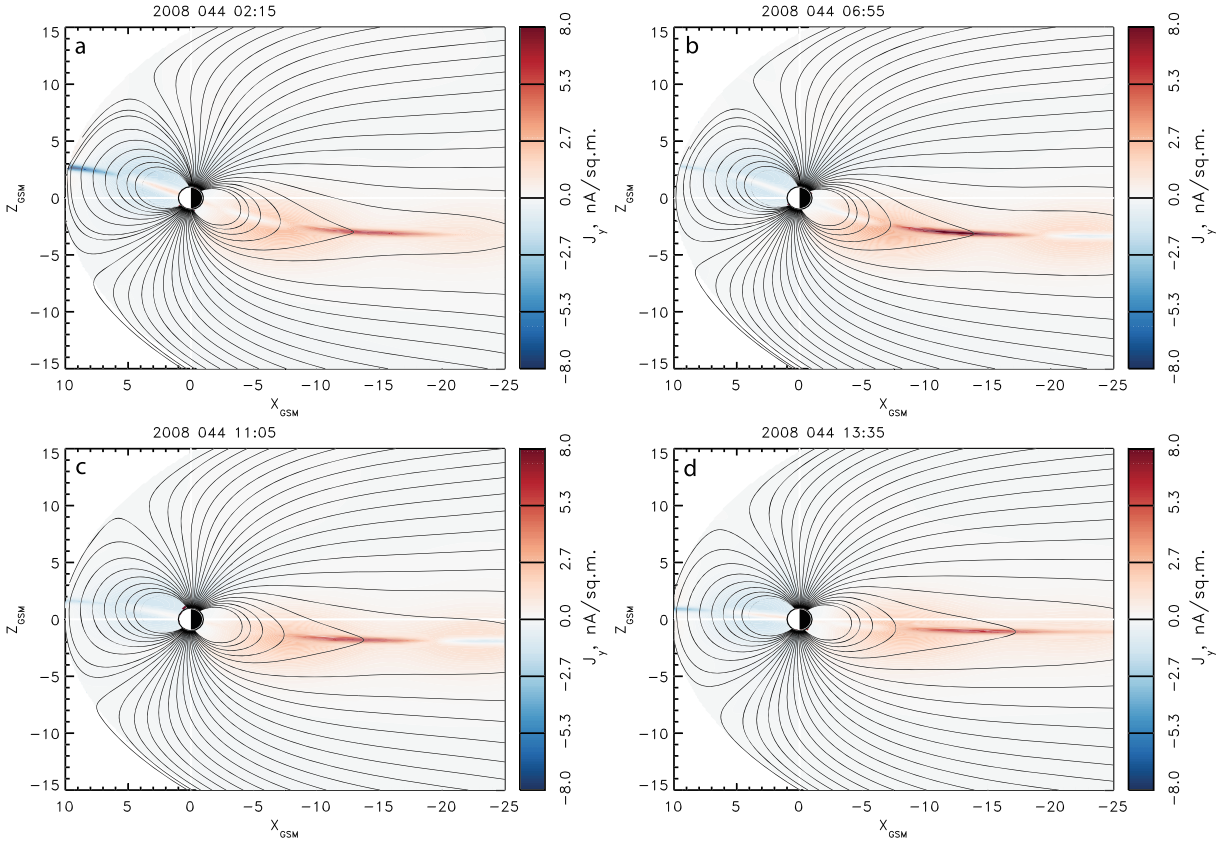

Figure 16. Distributions of the Y-component of the current density with overplotted magnetic field lines in the noon-midnight meridional plane for sample moments in the growth phases of the 13 February 2008 substorms featuring thin current sheets (TCSs) with anomalously large aspect ratios $L_x/L_z >\sim 50$ (with $L_z \sim 0.2R_E$, according to Figure 8e) with rather mild stretching factors $|B_x|/B_z <\sim 10$ (Figure 15).

retreat (Figure 17i). The equatorial distributions of the B_z field show that the X-line, which forms early in the growth phase, occupies a substantial part of the the tail (Figures 18b, 18c, and Figure S11). Moreover, Figure S11 shows signatures of a stagnant plasmoid, similar to those found in the middle tail (Nishida et al., 1986), which persists in the region $> 15R_E$ at least 30 min before substorm onset. This is confirmed by THEMIS observations, which show negative and then positive B_z excursions detected by probes B, C, D, and E (Figures S9 and S10). The stagnant nature of the plasmoid is also confirmed by THEMIS plasma observations (http://themis.ssl.berkeley.edu/index.shtml), which show surprisingly weak tailward ion flows during that period, with the largest values $\sim$ 100 km/s (probe B).

Still, as before, the onset is marked by a rapid decrease of the TCS amplitude (Figure 17f, orange line) and increase of the B_z field inside and outside geosynchronous orbit (Figure 17g). It is interesting that in this event, the major dipolarization occurs $\sim$ 30 min after the formation of the X-line (08:10 UT), and it takes almost an hour to complete (08:40-09:30 UT).

Supporting Figure S12 shows that the strong tail current (> 20 nA/m^2) first splits near the midnight meridian into two filaments (Figure S12b) and later decays (Figure S12c). Panels (d) in Figures 18, S12, and S13 describe the magnetosphere deep in the recovery phase when the TCS is rebuilt (see also the solid orange line in Figure 17f) whereas the X-line inside $20R_E$ region disappears.

The obtained near-Earth location of the new X-line in this case is consistent with earlier statistical investigations based on Geotail, Cluster, and THEMIS data (Imber et al., 2011; Miyashita et al., 2004; Nagai et al., 2005) that showed a weak dependence of the X-line location on the solar wind electric field parameter vB_z^{IMF}. Here the new finding made with the DM approach is that in this strongly driven regime the new X-line forms relatively early in the growth phase, but the reconnection process remains slow for half an hour before the substorm onset time (08:10-08:40 UT in Figure 17h).

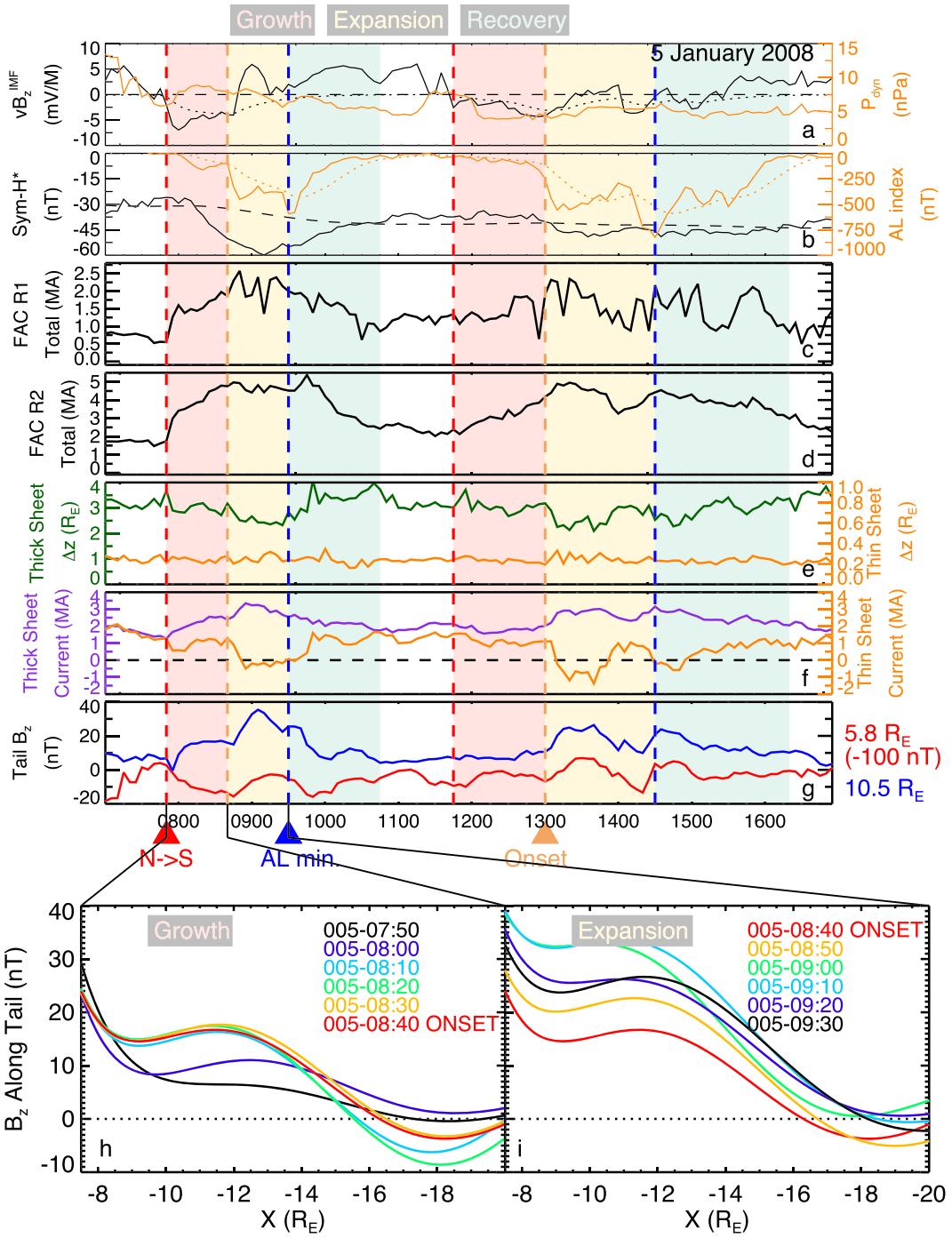

Figure 17. Analysis of the 5 January 2008 substorms in the format similar to Figure 4. Panels (h and i) show the evolution of the B_z field in growth and expansion phases of the substorm.

7. Further Error Analysis

We discussed above several substorms with the largest coverage of in situ observations along the tail provided by the THEMIS mission. More detailed validation in space is inherently difficult because the detailed spatial description of these substorms only becomes possible through the present SSTDM approach. However, one can evaluate the fidelity of SSTDM itself by comparing the observed values of the state parameters G_1 - G_5 with their NN means and standard deviations. Here we limit the analysis to the last three of these DM

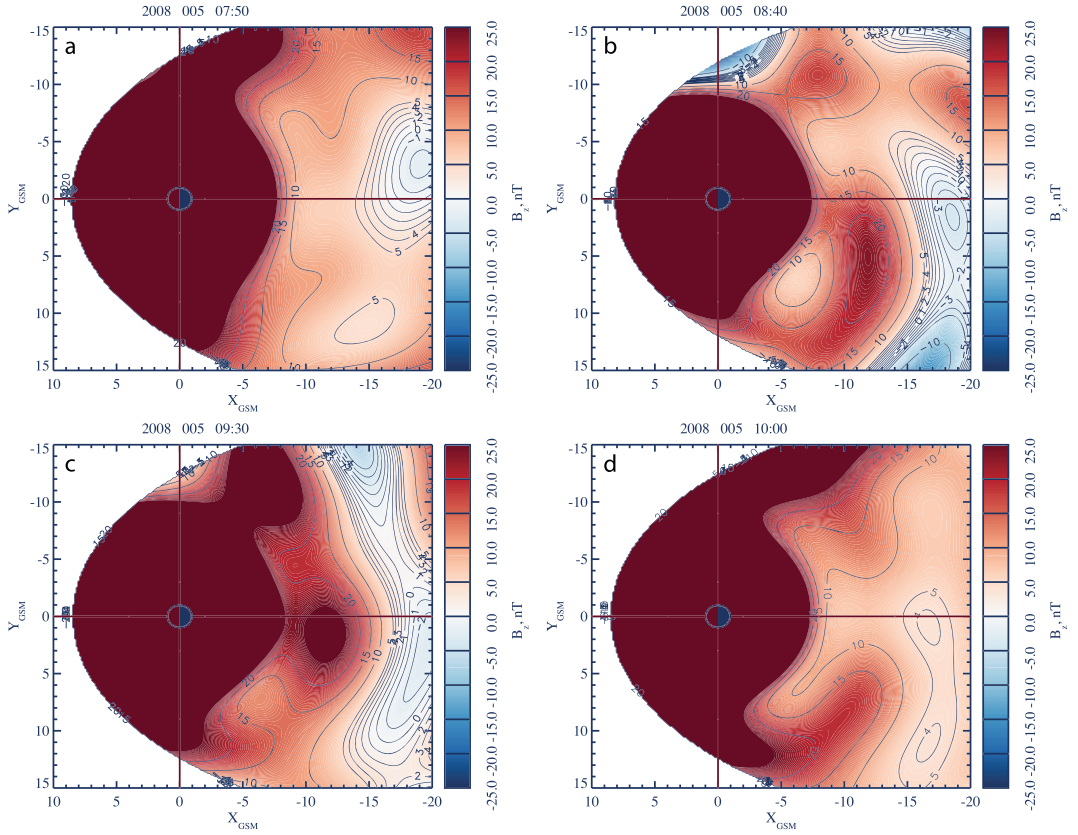

Figure 18. Distributions of the equatorial magnetic field B_z (using zero tilt angle) for the first of two 5 January 2008 substorms in the format similar to Figure 2g: (a - b) growth phase, (c - d) expansion and recovery phases.

state parameters of the magnetosphere taking into account that the substorms considered above occurred in periods of weak storm activity.

Figures 19a-19c show that the means over $K_{NN} = 32,000$ NNs of the substorm binning parameters G_3–G_5 for first three 13 February 2008 substorms differ from the original parameters G_3–G_5 rather slightly. Even for the fourth event with $AL_{\min} \approx -600$nT, the deviation in the parameter G_3 (the nowcasting time-averaged AL) is only 25%. At the same time, this NN-mean analysis reveals that one can expect strong relative errors in modeling of the late recovery phase, because of the overestimation of the solar wind binning parameter G_5. The latter is likely caused by time averaging of the solar wind noise occurring on the scales below those of substorms. These deviations are still rather small compared to the peak values of the solar wind electric field. Therefore they should not critically affect the reconstruction of the key substorm features.

Stronger (up to 30%) deviations of the NN-means (red lines) from the actual values (black lines) of the solar wind parameter G_5 are found for the first of the 5 January 2008 substorms (Figure 19f), which is described in the previous section. They suggest that events with such a strong driving are the relatively rare phenomena, and they explain the relatively poor validation results obtained for that example of strongly-driven substorms (Figures S9 and S10). At the same time, good consistency between the original values of the parameters G_3 and G_4, which reflects the substorm state of the magnetosphere, and their NN means suggests that the SSTDM reconstruction of the January 5, 2008 substorms should properly reflect key features of these events.

The picture of standard deviations (blue lines in Figure 19), compared to the original binning parameters G_3 - G_5 as well as their NN means, suggests that statistical errors caused by averaging of the magnetospheric dynamics over the NN bins of $K_{NN} = 32,000$ points are much smaller compared to major variations of these parameters during the presented substorms. Therefore the empirical picture of the magnetic field and its variations during substorms described above should reflect characteristic features of the magnetosphere during these events. Relatively strong standard deviations for the solar wind parameter G_5 (especially for the first, third, and fourth events in Figure 19c) suggest that the solar wind variations are less coherent and

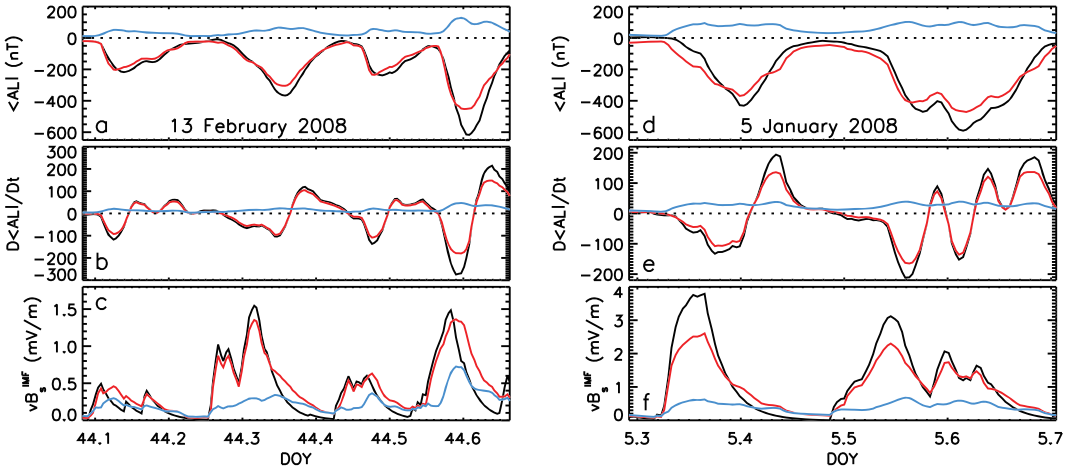

Figure 19. The substorm part of the original binning parameters (3)–(5) (black lines), their averages, and standard deviations over the NN subsets ($K_{NN} = 32,000$) shown by red and blue lines, respectively, for 13 February 2008 (a–c) and 5 January 2008 (d–f) groups of substorms. Parameters $\langle AL|$ and $\langle vB_s^{IMF}|$ are smoothed by their time averaging functions $\langle \ldots |$ defined by (3) and (5).

reproducible, compared to the dynamics of the ionospheric electrojets, which is consistent with the known turbulent nature of the solar wind (e.g., Bruno & Carbone, 2013).

8. Discussion and Conclusion

In this study we applied data mining and machine learning algorithms termed SSTDM (Stephens et al., 2019) to investigate regions and processes associated with nonideal (different from isotropic MHD) behavior of plasma and including (but not limited to) the formation of X-lines. The latter are formed mainly at and beyond 20 R_E, where the data density distribution of the pre-MMS database rapidly dropped. Thus, the new MMS data have become critically important in the reconstruction of reconnection effects. In particular, it becomes possible to reconstruct the global structure of the X-line (Figure 2g) associated with the electron diffusion regions observed by the MMS on 11 July 2017 (Torbert et al., 2018).

It is found that the formation of X-lines may be preceded by redistribution of the magnetic flux in the tailward B_z gradient regions (Figure 5i), the process, which was predicted a decade ago in the theory of the tearing instability and then found in PIC and MHD simulations of ad hoc magnetotail equilibria containing TGRs. Note that finding configurations with such metastable TGRs (Figures 5h and 8h) is rather unexpected, and it poses another challenge for theory and simulations, because the redistribution of flux along the tail should compete with buoyancy-driven interchange plasma motions. Moreover, according to the present MHD theory, the threshold of interchange instabilities is lower, compared to tearing (Schindler & Birn, 2004).

It is also found that current sheets in the growth phase may become as thin as 0.2 R_E, comparable to the thermal ion gyroradius, and at the same time, as long as 15 R_E. Quantitative estimates of the ratio between the equatorial B_z and lobe field B_0, approximated by the field B_x at $z = 5R_E$ (Figure 15), show that the found TCS aspect ratios L_x/L_z up to ~ 75 (Figure 16) are inconsistent with the isotropic force balance condition for observed magnetic field configurations with $B_0/B_z \sim 10$. Thus, potential deviations from the ideal isotropic MHD approximation during substorms are not limited to X-lines, and they may also include thin anisotropic and agyrotropic TCSs as well as TGRs.

The analysis of the magnetic flux evolution in the substorm expansion phase (Figure 13) reveals that the corresponding reconnection process is inherently unsteady. Therefore, the reconnection electric field distribution should be inhomogeneous. Indeed, while the near-Earth magnetic field dipolarization is accomplished as quickly as in ~ 5 min (the highest time resolution of the present reconstruction technique), the lobe flux redistribution proceeds relatively slowly to replenish the dipolarized flux during the recovery and next growth phases. At the same time, the main part of the near-Earth dipolarization can be provided by the redistribution of magnetic flux in the closed field line region (Figure 14).

Finally, it is found that for relatively strong driving, with the solar wind electric field exceeding $\sim$ 5 mV/m and the dynamic pressure $\sim$ 7 nPa, the X-line may form as close as at $\approx 15R_E$ already 30 min before substorm onset. This regime is featured by the formation of a stagnant plasmoid (Nishida et al., 1986) with very weak tailward plasma flows (not to exceed $\sim$ 100 km/s in amplitude). It is followed by a relatively long ($\sim$ 1 hr) expansion phase with slow dipolarization.

This analysis is rather global and as such it complements the microscale kinetic studies of nonideal effects in substorms (e.g., Torbert et al., 2018). Moreover, it can guide such microscale investigations pointing to X-lines and TCSs. In case of TGRs, the microscale analysis can be used to distinguish between their ideal MHD evolution (Birn et al., 2018; Merkin et al., 2015) and kinetic regimes (Bessho & Bhattacharjee, 2014; Pritchett, 2015; Sitnov et al., 2013).

The obtained empirical picture of X-lines, TCSs, and TGRs can also be used to improve the first-principles models as it reveals the regimes and regions with nonideal evolution and suggests possible improvements for their description. In particular, it suggests that for the description of TCSs in the growth phase it is necessary to extend the isotropic MHD description of the magnetotail taking anisotropic and nongyrotropic corrections into account or to employ a hybrid description of plasmas with kinetic ions and fluid electron species. Embedded PIC setups may be a relevant model for substorms with strong solar wind driving (section 6), whereas for the description of spontaneous reconnection onsets in case of weaker solar wind driving different models must be elaborated to account for the formation of TCSs and TGRs.

It is important to note that the present MHD codes, either due to numerical effects or explicit resistivity, already effectively capture some nonideal effects, such as the X-line formation (e.g., Raeder et al., 2008). They describe quite thin current sheets (e.g., Wiltberger et al., 2000) and TGR features (Garcia-Sage et al., 2016; Otto et al., 2015; Sergeev et al., 2018). It is possible therefore that the consistency with the observed nonideal features can be achieved through systematic comparison of the empirical and MHD results and the formation of the empirical dependencies of the numerical parameters, such as the code resolution or explicit resistivity, on the substorm activity level and its trends.

It is necessary to take into account that the nonideal features of X-lines, TCSs, and TGRs do not necessarily imply that these regions exhibit energy dissipation or finite conductivity. They can exist as fully self-consistent collisionless plasma equilibria (e.g., Sitnov & Merkin, 2016, and refs. therein), and they can be both stable and unstable (e.g., Sitnov et al., 2013). In these equilibria, both the conventional MHD Joule heating rate (e.g., Birn & Hesse, 2014, and refs. therein) and kinetic dissipation parameters (Sitnov et al., 2018) can be equal to zero, because of the zero electric field in the former case and zero bulk plasma flow, in the latter.

Revealing nonideal effects in the empirical picture of substorms can also help build future generations of MHD models with explicit kinetic corrections. The comprehensive kinetic description of the magnetosphere remains challenging: Explicit PIC codes are not feasible (e.g., Lapenta, 2012, and refs. therein), and even global implicit and hybrid codes (e.g., Lin et al., 2014) must resolve the ion gyroradius scale. More feasible simulations have to couple MHD and kinetic descriptions. But such a coupling still involves critical ad hoc assumptions. For example, in embedded PIC simulations (e.g., Daldorff et al., 2014), it is assumed that the location of the new X-line in the tail is known from the large-scale MHD simulations. However, this may or may not be true, because MHD models do not capture the kinetic physics of the magnetotail reconnection onset(Sitnov et al., 2019, and refs. therein) and therefore the location and timing of the X-line formation may deviate from observations (e.g., Raeder et al., 2008). Here the empirical picture of nonideal phenomena can be used to either adjust the location and timing of the X-line formation in cases of the strong driving (section 6) or identify more extended areas with TCS and TGR features. The latter could be simulated using single-particle tracing of the high-energy tails of plasma velocity distributions (e.g., Sorathia et al., 2018) with subsequent kinetic corrections of the MHD description (e.g., Mignone et al., 2018).

Further SSTDM analysis may include not only more events and substorm regimes but also an improvement of the binning space (1)-(5). In particular, the IMF B_y component may modify the dayside reconnection and hence the energy input into the magnetosphere, penetrate the magnetotail, causing its tilt, and substantially modify the whole substorm picture(e.g., Ohma et al., 2018, and refs. therein). The effects of the IMF B_y have already been addressed in earlier STDM analysis of storm-scale evolution using the extension of the 3-D STDM binning space to four dimensions (Sitnov et al., 2017). Their investigation on the substorm level

may require either the use of more general input parameters, taking the IMF clock angle into account (e.g., Perreault & Akasofu, 1978), or some trade-off in the selection of the binning space parameters (1)–(5). For example one can use the substorm state parameters (3)–(5) only, together with the IMF B_y parameter similar to (Sitnov et al., 2017). Further advance may also be provided due to the replacement of the classical storm and substorm indices $Sym-H$ and AL by their recent modifications based on SuperMag data (Newell & Gjerloev, 2011, 2012).

Acknowledgments
This work was funded by NASA grants NNX16AB78G, NNX16AB80G, and 80NSSC19K0074 as well as NSF grants AGS-1702147 and AGS-1744269. We thank the many spacecraft and instrument teams and their PIs who produced the data sets we used in this study, including the Cluster, Geotail, Polar, IMP-8, GOES, THEMIS, Van Allen Probes, and MMS, particularly their magnetometer teams. We also thank the SPDF for the OMNI database for solar wind values, which is composed of data sets from the IMP-8, ACE, WIND, and Geotail missions, and also the WDC in Kyoto for the Geomagnetic indices. We also want to thank Joachim Birn, James Burch, Paul Cassak, Matina Gkioulidou, Steven Milan, Rumi Nakamura, Fulvia Pucci, Andrei Runov, Victor Sergeev, Marc Swisdak, and Aleksandr Ukhorskiy for useful discussions. The 3-D visualizations were performed using VisIt, which is supported by the Department of Energy with funding from the Advanced Simulation and Computing Program and the Scientific Discovery through Advanced Computing Program. The data and data products related to the paper are archived on Zenodo (https://doi.org/10.5281/zenodo.3364704).

References

Alfvén, H. (1942). Existence of electromagnetic-hydrodynamic waves. *Nature*, *150*, 405–406. https://doi.org/10.1038/150405d0

Anderson, B. J., Olson, C. N., Korth, H., Barnes, R. J., Waters, C. L., & Vines, S. K. (2018). Temporal and spatial development of global Birkeland currents. *Journal of Geophysical Research: Space Physics*, *123*, 4785–4808. https://doi.org/10.1029/2018JA025254

Angelopoulos, V., Runov, A., Zhou, X.-Z., Turner, D. L., Kiehas, S. A., Li, S. S., & Shinohara, I. (2013). Electromagnetic energy conversion at reconnection fronts. *Science*, *341*(6153), 1478–1482. https://doi.org/10.1126/science.1236992

Artemyev, A. V., Angelopoulos, V., Runov, A., & Petrukovich, A. A. (2019). Global view of current sheet thinning: Plasma pressure gradients and large-scale currents. *Journal of Geophysical Research: Space Physics*, *124*, 264–278. https://doi.org/10.1029/2018JA026113

Artemyev, A. V., Petrukovich, A. A., Nakamura, R., & Zelenyi, L. M. (2015). Two-dimensional configuration of the magnetotail current sheet: THEMIS observations. *Geophysical Research Letters*, *42*, 3662–3667. https://doi.org/10.1002/2015GL063994

Asano, Y., Mukai, T., Hoshino, M., Saito, Y., Hayakawa, H., & Nagai, T. (2004). Statistical study of thin current sheet evolution around substorm onset. *Journal of Geophysical Research*, *109*, A05213. https://doi.org/10.1029/2004JA010413

Asano, Y., Nakamura, R., Baumjohann, W., Runov, A., Vörös, Z., Volwerk, M, et al. (2005). How typical are atypical current sheets?. *Geophysical Research Letters*, *32*, L03108. https://doi.org/10.1029/2004GL021834

Baker, D. N., Pulkkinen, T. I., Angelopoulos, V., Baumjohann, W., & McPherron, R. L. (1996). Neutral line model of substorms: Past results and present view. *Journal of Geophysical Research*, *101*(A6), 12,975–13,010. https://doi.org/10.1029/95JA03753

Baumjohann, W., Paschmann, G., & Lühr, H. (1990). Characteristics of high-speed ion flows in the plasma sheet. *Journal of Geophysical Research*, *95*(A4), 3801–3809. https://doi.org/10.1029/JA095iA04p03801

Bessho, N., & Bhattacharjee, A. (2014). Instability of the current sheet in the Earth's magnetotail with normal magnetic field. *Physics of Plasmas*, *21*(10), 102905. https://doi.org/10.1063/1.4899043

Birn, J., Drake, J. F., Shay, M. A., Rogers, B. N., Denton, R. E., Hesse, M., et al. (2001). Geospace environmental Modeling (GEM) Magnetic Reconnection Challenge. *Journal of Geophysical Research*, *106*(A3), 3715–3719. https://doi.org/10.1029/1999JA900449

Birn, J., & Hesse, M. (2014). Forced reconnection in the near magnetotail: Onset and energy conversion in PIC and MHD simulations. *Journal of Geophysical Research: Space Physics*, *119*, 290–309. https://doi.org/10.1002/2013JA019354

Birn, J., Merkin, V. G., Sitnov, M. I., & Otto, A. (2018). MHD stability of magnetotail configurations with a B_z hump. *Journal of Geophysical Research: Space Physics*, *123*, 3477–3492. https://doi.org/10.1029/2018JA025290

Birn, J., Schindler, K., & Hesse, M. (2003). Formation of thin current sheets in the magnetotail: Effects of propagating boundary deformations. *Journal of Geophysical Research*, *108*(A9), 1337. https://doi.org/10.1029/2002JA009641

Bruno, R., & Carbone, V. (2013). The solar wind as a turbulence laboratory. *Living Reviews in Solar Physics*, *10*(1), 2. https://doi.org/10.12942/lrsp-2013-2

Burch, J. L., & Phan, T. D. (2016). Magnetic reconnection at the dayside magnetopause: Advances with MMS. *Geophysical Research Letters*, *43*, 8327–8338. https://doi.org/10.1002/2016GL069787

Cassak, P. A., Liu, Y.-H., & Shay, M. (2017). A review of the 0.1 reconnection rate problem. *Journal of Plasma Physics*, *83*(5), 715830501. https://doi.org/10.1017/S0022377817000666

Chen, L.-J., Wang, S., Hesse, M., Ergun, R. E., Moore, T., Giles, B., et al. (2019). Electron diffusion regions in magnetotail reconnection under varying guide fields. *Geophysical Research Letters*, *46*, 6230–6238. https://doi.org/10.1029/2019GL082393

Cole, G. H. A., & Schindler, K. (1972). On the equilibrium configuration of the geomagnetic tail. *Cosmic Electrodynamics*, *3*, 275–284.

Cover, T., & Hart, P. (1967). Nearest neighbor pattern classification. *IEEE Transactions on Information Theory*, *13*(1), 21–27. https://doi.org/10.1109/TIT.1967.1053964

Cowley, S. (1978). The effect of pressure anisotropy on the equilibrium structure of magnetic current sheets. *Planetary and Space Science*, *26*(11), 1037–1061. https://doi.org/10.1016/0032-0633(78)90028-4

Daldorff, L. K. S., Tóth, G., Gombosi, T. I., Lapenta, G., Amaya, J., Markidis, S., & Brackbill, J. U. (2014). Two-way coupling of a global Hall magnetohydrodynamics model with a local implicit particle-in-cell model. *Journal of Computational Physics*, *268*, 236–254. https://doi.org/10.1016/j.jcp.2014.03.009

Dungey, J. W. (1961). Interplanetary magnetic field and the Auroral Zones. *Physical Review Letters*, *6*, 47–48. https://doi.org/10.1103/PhysRevLett.6.47

Eastwood, J. P., Nakamura, R., Turc, L., Mejnertsen, L., & Hesse, M. (2017). The scientific foundations of forecasting magnetospheric space weather. *Space Science Reviews*, *212*(3), 1221–1252. https://doi.org/10.1007/s11214-017-0399-8

Eastwood, J. P., Phan, T. D., Øieroset, M., & Shay, M. A. (2010). Average properties of the magnetic reconnection ion diffusion region in the Earth's magnetotail: The 2001-2005 Cluster observations and comparison with simulations. *Journal of Geophysical Research*, *115*, A08215. https://doi.org/10.1029/2009JA014962

Fuselier, S. A., Trattner, K. J., & Petrinec, S. M. (2011). Antiparallel and component reconnection at the dayside magnetopause. *Journal of Geophysical Research*, *116*, A10227. https://doi.org/10.1029/2011JA016888

Galeev, A. A. (1984). Spontaneous reconnection of magnetic field lines in a collisionless plasma. In A. A. Galeev, & R. N. Sudan (Eds.), *Handbook of Plasma Physics* (Vol. 2, pp. 305–335). North-Holland, New York: Elsevier Science Publishing Company, Inc.

Garcia-Sage, K., Merkin, V. G., Sitnov, M. I., Moore, T. E., & Pembroke, A. D. (2016). Magnetotail stability parameters in global MHD simulations. *Fall AGU Meeting, Presentation SM41B-2426*.

Genestreti, K. J., Nakamura, T. K. M., Nakamura, R., Denton, R. E., Torbert, R. B., Burch, J. L., et al. (2018). How accurately can we measure the reconnection rate E_m for the MMS diffusion region event of 11 July 2017? *Journal of Geophysical Research: Space Physics*, *123*, 9130–9149. https://doi.org/10.1029/2018JA025711

Gordeev, E., Sergeev, V., Honkonen, I., Kuznetsova, M., Rastätter, L., Palmroth, M., et al. (2015). Assessing the performance of community-available global MHD models using key system parameters and empirical relationships. *Space Weather*, *13*, 868–884. https://doi.org/10.1002/2015SW001307

Harang, L. (1946). The mean field of disturbance of polar geomagnetic storms. *Terrestrial Magnetism and Atmospheric Electricity*, *51*(3), 353–380. https://doi.org/10.1029/TE051i003p00353

Hesse, M., & Schindler, K. (2001). The onset of magnetic reconnection in the magnetotail. *Earth, Planets and Space*, *53*, 645–653.

Hones, E. W. (1979). Transient phenomena in the magnetotail and their relation to substorms. *Space Science Reviews*, *23*(3), 393–410. https://doi.org/10.1007/BF00172247

Hones, E. W. Jr. (1984). Plasma sheet behavior during substorms, *Magnetic Reconnection in Space and Laboratory Plasmas* (pp. 178–184). Washington, DC: American Geophysical Union . https://doi.org/10.1029/GM030p0178

Ieda, A., Machida, S., Mukai, T., Saito, Y., Yamamoto, T., Nishida, A., et al. (1998). Statistical analysis of the plasmoid evolution with Geotail observations. *Journal of Geophysical Research*, *103*(A3), 4453–4465. https://doi.org/10.1029/97JA03240

Iijima, T., & Potemra, T. A. (1976). The amplitude distribution of field-aligned currents at northern high latitudes observed by Triad. *Journal of Geophysical Research*, *81*(13), 2165–2174. https://doi.org/10.1029/JA081i013p02165

Imber, S. M., Slavin, J. A., Auster, H. U., & Angelopoulos, V. (2011). A THEMIS survey of flux ropes and traveling compression regions: Location of the near-Earth reconnection site during solar minimum. *Journal of Geophysical Research*, *116*, A02201. https://doi.org/10.1029/2010JA016026

Ji, H., & Daughton, W. (2011). Phase diagram for magnetic reconnection in heliophysical, astrophysical, and laboratory plasmas. *Physics of Plasmas*, *18*(11), 11,1207–11,1207. https://doi.org/10.1063/1.3647505

Kivelson, M., & Russell, C. (1995). *Introduction to Space Physics*. Cambridge, UK: Cambridge University Press. https://books.google.com/books?id=DIybBQAAQBAJ

Koskinen, H. E. J., Lopez, R. E., Pellinen, R. J., Pulkkinen, T. I., Baker, D. N., & Bösinger, T. (1993). Pseudobreakup and substorm growth phase in the ionosphere and magnetosphere. *Journal of Geophysical Research*, *98*(A4), 5801–5813. https://doi.org/10.1029/92JA02482

Koskinen, H. E. J., & Pulkkinen, T. I. (1995). Midnight velocity shear zone and the concept of Harang discontinuity. *Journal of Geophysical Research*, *100*(A6), 9539–9547. https://doi.org/10.1029/95JA00228

Kubat, M. (2015). *An introduction to machine learning* (1st ed). Switzerland: Springer Publishing Company, Incorporated.

Kubyshkina, M. V., Sergeev, V. A., & Pulkkinen, T. I. (1999). Hybrid input algorithm: An event-oriented magnetospheric model. *Journal of Geophysical Research*, *104*(A11), 24,977–24,993. https://doi.org/10.1029/1999JA900222

Lapenta, G. (2012). Particle simulations of space weather. *Journal of Computational Physics*, *231*(3), 795–821. https://doi.org/10.1016/j.jcp.2011.03.035

Le Contel, O., Nakamura, R., Breuillard, H., Argall, M. R., Graham, D. B., Fischer, D., et al. (2017). Lower hybrid drift waves and electromagnetic electron space-phase holes associated with dipolarization fronts and field-aligned currents observed by the Magnetospheric Multiscale mission during a substorm. *Journal of Geophysical Research: Space Physics*, *122*, 12,236–12,257. https://doi.org/10.1002/2017JA024550

Li, S.-S., Liu, J., Angelopoulos, V., Runov, A., Zhou, X.-Z., & Kiehas, S. A. (2014). Antidipolarization fronts observed by ARTEMIS. *Journal of Geophysical Research: Space Physics*, *119*, 7181–7198. https://doi.org/10.1002/2014JA020062

Lin, Y., Wang, X. Y., Lu, S., Perez, J. D., & Lu, Q. (2014). Investigation of storm time magnetotail and ion injection using three-dimensional global hybrid simulation. *Journal of Geophysical Research: Space Physics*, *119*, 7413–7432. https://doi.org/10.1002/2014JA020005

Lu, S., Lin, Y., Angelopoulos, V., Artemyev, A. V., Pritchett, P. L., Lu, Q., & Wang, X. Y. (2016). Hall effect control of magnetotail dawn-dusk asymmetry: A three-dimensional global hybrid simulation. *Journal of Geophysical Research: Space Physics*, *121*, 11,882–11,895. https://doi.org/10.1002/2016JA023325

Lyon, J. G., Fedder, J. A., & Mobarry, C. M. (2004). The Lyon-Fedder-Mobarry (LFM) global MHD magnetospheric simulation code. *Journal of Atmospheric and Solar-Terrestrial Physics*, *66*, 1333–1350. https://doi.org/10.1016/j.jastp.2004.03.020

Machida, S., Miyashita, Y., Ieda, A., Nosé, M., Nagata, D., Liou, K., et al. (2009). Statistical visualization of the Earth's magnetotail based on Geotail data and the implied substorm model. *Annales Geophysicae*, *27*(3), 1035–1046. https://doi.org/10.5194/angeo-27-1035-2009

McPherron, R. L. (2016). Where and when does reconnection occur in the tail? *Journal of Geophysical Research: Space Physics*, *121*, 4607–4610. https://doi.org/10.1002/2015JA022258

Meng, X., Tóth, G., Glocer, A., Fok, M.-C., & Gombosi, T. I. (2013). Pressure anisotropy in global magnetospheric simulations: Coupling with ring current models. *Journal of Geophysical Research: Space Physics*, *118*, 5639–5658. https://doi.org/10.1002/jgra.50539

Meng, X., Tóth, G., Liemohn, M. W., Gombosi, T. I., & Runov, A. (2012). Pressure anisotropy in global magnetospheric simulations: A magnetohydrodynamics model. *Journal of Geophysical Research*, *117*, A08216. https://doi.org/10.1029/2012JA017791

Merkin, V. G., & Sitnov, M. I. (2016). Stability of magnetotail equilibria with a tailward B_z gradient. *Journal of Geophysical Research: Space Physics*, *121*, 9411–9426. https://doi.org/10.1002/2016JA023005

Merkin, V. G., Sitnov, M. I., & Lyon, J. G. (2015). Evolution of generalized two-dimensional magnetotail equilibria in ideal and resistive MHD. *Journal of Geophysical Research: Space Physics*, *120*, 1993–2014. https://doi.org/10.1002/2014JA020651

Mignone, A., Bodo, G., Vaidya, B., & Mattia, G. (2018). A particle module for the PLUTO Code. I. An implementation of the MHD–PIC Equations. *The Astrophysical Journal*, *859*(1), 13. https://doi.org/10.3847/1538-4357/aabccd

Milan, S. E., Grocott, A., Forsyth, C., Imber, S. M., Boakes, P. D., & Hubert, B. (2009). A superposed epoch analysis of auroral evolution during substorm growth, onset and recovery: Open magnetic flux control of substorm intensity. *Annales Geophysicae*, *27*(2), 659–668. https://doi.org/10.5194/angeo-27-659-2009

Miyashita, Y., Kamide, Y., Machida, S., Liou, K., Mukai, T., Saito, Y., et al. (2004). Difference in magnetotail variations between intense and weak substorms. *Journal of Geophysical Research*, *109*, A11205. https://doi.org/10.1029/2004JA010588

Miyashita, Y., Machida, S., Kamide, Y., Nagata, D., Liou, K., Fujimoto, M., et al. (2009). A state-of-the-art picture of substorm-associated evolution of the near-Earth magnetotail obtained from superposed epoch analysis. *Journal of Geophysical Research*, *114*, A01211. https://doi.org/10.1029/2008JA013225

Miyashita, Y., Machida, S., Mukai, T., Saito, Y., Tsuruda, K., Hayakawa, H., & Sutcliffe, P. R. (2000). A statistical study of variations in the near and middistant magnetotail associated with substorm onsets: GEOTAIL observations. *Journal of Geophysical Research*, *105*(A7), 15,913–15,930. https://doi.org/10.1029/1999JA000392

Nagai, T., Fujimoto, M., Nakamura, R., Baumjohann, W., Ieda, A., Shinohara, I., et al. (2005). Solar wind control of the radial distance of the magnetic reconnection site in the magnetotail. *Journal of Geophysical Research*, *110*, A09208. https://doi.org/10.1029/2005JA011207

Nakamura, R., Genestreti, K. J., Nakamura, T., Baumjohann, W., Varsani, A., Nagai, T., et al. (2019). Structure of the current sheet in the 11 July 2017 electron diffusion region event. *Journal of Geophysical Research: Space Physics*, *124*, 1173–1186. https://doi.org/10.1029/2018JA026028

Nakamura, T. K. M., Nakamura, R., Varsani, A., Genestreti, K. J., Baumjohann, W., & Liu, Y.-H. (2018). Remote sensing of the reconnection electric field from in situ multipoint observations of the separatrix boundary. *Geophysical Research Letters*, *45*, 3829–3837. https://doi.org/10.1029/2018GL078340

Newell, P. T., & Gjerloev, J. W. (2011). Evaluation of superMAG auroral electrojet indices as indicators of substorms and auroral power. *Journal of Geophysical Research*, *116*, A12211. https://doi.org/10.1029/2011JA016779

Newell, P. T., & Gjerloev, J. W. (2012). SuperMAG-based partial ring current indices. *Journal of Geophysical Research*, *117*, A05215. https://doi.org/10.1029/2012JA017586

Nishida, A., Scholer, M., Terasawa, T., Bame, S. J., Gloeckler, G., Smith, E. J., & Zwickl, R. D. (1986). Quasi-stagnant plasmoid in the middle tail: A new preexpansion phase phenomenon. *Journal of Geophysical Research*, *91*(A4), 4245–4255. https://doi.org/10.1029/JA091iA04p04245

Ohma, A., Østgaard, N., Reistad, J. P., Tenfjord, P., Laundal, K. M., Snekvik, K., et al. (2018). Evolution of asymmetrically displaced footpoints during substorms. *Journal of Geophysical Research: Space Physics*, *123*, 10,030–10,063. https://doi.org/10.1029/2018JA025869

Ohtani, S., & Motoba, T. (2017). Equatorial magnetic field of the near-Earth magnetotail. *Journal of Geophysical Research: Space Physics*, *122*, 8462–8478. https://doi.org/10.1002/2017JA024115

Ohtani, S., & Mukai, T. (2008). Statistical characteristics of the storm time plasma sheet. *Journal of Geophysical Research*, *113*, A01221. https://doi.org/10.1029/2007JA012547

Ohtani, S., Takahashi, K., Zanetti, L. J., Potemra, T. A., McEntire, R. W., & Iijima, T. (1991). Tail current disruption in the geosynchronous region, *Magnetospheric Substorms* (pp. 131–137). Washington, DC: American Geophysical Union. https://doi.org/10.1029/GM064p0131

Ohtani, S., Yamaguchi, R., Nosé, M., Kawano, H., Engebretson, M., & Yumoto, K. (2002). Quiet time magnetotail dynamics and their implications for the substorm trigger. *Journal of Geophysical Research*, *107*(A2), 1030. https://doi.org/10.1029/2001JA000116

Otto, A., Hsieh, M.-S., & Hall, F. (2015). Current sheet formation in planetary magnetotails, *Magnetotails in the Solar System* (pp. 289–305). Hoboken, NJ, USA: John Wiley Inc. https://doi.org/10.1002/9781118842324.ch17

Partamies, N., Juusola, L., Tanskanen, E., & Kauristie, K. (2013). Statistical properties of substorms during different storm and solar cycle phases. *Annales Geophysicae*, *31*(2), 349–358. https://doi.org/10.5194/angeo-31-349-2013

Perreault, P., & Akasofu, S.-I. (1978). A study of geomagnetic storms. *Geophysical Journal of the Royal Astronomical Society*, *54*(3), 547–573. https://doi.org/10.1111/j.1365-246X.1978.tb05494.x

Petrukovich, A. A., Artemyev, A. V., Nakamura, R., Panov, E. V., & Baumjohann, W. (2013). Cluster observations of dBz/dx during growth phase magnetotail stretching intervals. *Journal of Geophysical Research: Space Physics*, *118*, 5720–5730. https://doi.org/10.1002/jgra.50550

Pritchett, P. L. (2015). Instability of current sheets with a localized accumulation of magnetic flux. *Physics of Plasmas*, *22*, 62102. https://doi.org/10.1063/1.4921666

Pulkkinen, T. I., Baker, D. N., Cogger, L. L., Mukai, T., & Singer, H. J. (1998). Coupling of inner tail and midtail processes. In S. Kokubun, & Y. Kamide (Eds.), *Substorms-4* (pp. 749–754). Dordrecht, London, Boston: Kluwer Acad. Publ.

Pulkkinen, T. I., Baker, D. N., Fairfield, D. H., Pellinen, R. J., Murphree, J. S., Elphinstone, R. D., et al. (1991). Modeling the growth phase of a substorm using the Tsyganenko Model and multi-spacecraft observations: CDAW-9. *Geophysical Research Letters*, *18*(11), 1963–1966. https://doi.org/10.1029/91GL02002

Raeder, J., Larson, D., Li, W., Kepko, E. L., & Fuller-Rowell, T. (2008). OpenGGCM Simulations for the THEMIS Mission. *Space Science Reviews*, *141*(1–4), 535–555. https://doi.org/10.1007/s11214-008-9421-5

Rich, F. J., Vasyliunas, V. M., & Wolf, R. A. (1972). On the balance of stresses in the plasma sheet. *Journal of Geophysical Research*, *77*(25), 4670–4676. https://doi.org/10.1029/JA077i025p04670

Runov, A., Baumjohann, W., Nakamura, R., Sergeev, V. A., Amm, O., Frey, H., et al. (2008). Observations of an active thin current sheet. *Journal of Geophysical Research*, *113*, A07S27. https://doi.org/10.1029/2007JA012685

Saito, M. H., Fairfield, D., Le, G., Hau, L.-N., Angelopoulos, V., McFadden, J. P., et al. (2011). Structure, force balance, and evolution of incompressible cross-tail current sheet thinning. *Journal of Geophysical Research*, *116*, A10217. https://doi.org/10.1029/2011JA016654

Schindler, K. (1972). A selfconsistent theory of the tail of the magnetosphere. In B. M. McCormac (Ed.), *Earth's Magnetospheric Processes* (pp. 200–209). Dordrecht-Holland: D. Reidel.

Schindler, K. (1974). A theory of the substorm mechanism. *Journal of Geophysical Research*, *79*(19), 2803–2810. https://doi.org/10.1029/JA079i019p02803

Schindler, K. (2007). *Physics of Space Plasma Activity*. New York: Cambridge University Press.

Schindler, K., & Birn, J. (2004). MHD stability of magnetotail equilibria including a background pressure. *Journal of Geophysical Research*, *109*, A10208. https://doi.org/10.1029/2004JA010537

Sergeev, V. A., Gordeev, E. I., Merkin, V. G., & Sitnov, M. I. (2018). Does a Local B-Minimum Appear in the Tail Current Sheet During a Substorm Growth Phase? *Geophysical Research Letters*, *45*, 2566–2573. https://doi.org/10.1002/2018GL077183

Sergeev, V. A., Mitchell, D. G., Russell, C. T., & Williams, D. J. (1993). Structure of the tail plasma/current sheet at ~11 R_E and its changes in the course of a substorm. *Journal of Geophysical Research*, *98*, 17,345–17,365.

Sergeev, V. A., Pellinen, R. J., & Pulkkinen, T. I. (1996). Steady magnetospheric convection: A review of recent results. *Space Science Reviews*, *75*(3), 551–604. https://doi.org/10.1007/BF00833344

Shay, M. A., Drake, J. F., Rogers, B. N., & Denton, R. E. (1999). The scaling of collisionless, magnetic reconnection for large systems. *Geophysical Research Letters*, *26*(14), 2163–2166. https://doi.org/10.1029/1999GL900481

Sitnov, M., Birn, J., Ferdousi, B., Gordeev, E., Khotyaintsev, Y., Merkin, V., et al. (2019). Explosive Magnetotail Activity. *Space Science Reviews*, *215*(4), 31. https://doi.org/10.1007/s11214-019-0599-5

Sitnov, M. I., Buzulukova, N., Swisdak, M., Merkin, V. G., & Moore, T. E. (2013). Spontaneous formation of dipolarization fronts and reconnection onset in the magnetotail. *Geophysical Research Letters*, *40*, 22–27. https://doi.org/10.1029/2012GL054701

Sitnov, M. I., & Merkin, V. G. (2016). Generalized magnetotail equilibria: Effects of the dipole field, thin current sheets, and magnetic flux accumulation. *Journal of Geophysical Research: Space Physics*, *121*, 7664–7683. https://doi.org/10.1002/2016JA023001

Sitnov, M. I., Merkin, V. G., Pritchett, P. L., & Swisdak, M. (2017). Distinctive features of internally driven magnetotail reconnection. *Geophysical Research Letters*, *44*, 3028–3037. https://doi.org/10.1002/2017GL072784

Sitnov, M. I., Merkin, V. G., Roytershteyn, V., & Swisdak, M. (2018). Kinetic dissipation around a dipolarization front. *Geophysical Research Letters*, *45*, 4639–4647. https://doi.org/10.1029/2018GL077874

Sitnov, M. I., Merkin, V. G., Swisdak, M., Motoba, T., Buzulukova, N., Moore, T. E., et al. (2014). Magnetic reconnection, buoyancy and flapping motions in magnetotail explosions. *Journal of Geophysical Research: Space Physics*, *119*, 7151–7168. https://doi.org/10.1002/2014JA020205

Sitnov, M. I., & Schindler, K. (2010). Tearing stability of a multiscale magnetotail current sheet. *Geophysical Research Letters*, *37*, L08102. https://doi.org/10.1029/2010GL042961

Sitnov, M. I., Stephens, G. K., Gkioulidou, M., Merkin, V., Ukhorskiy, A. Y., Korth, H., et al. (2018). Chapter 11 - Empirical modeling of extreme events: Storm-time geomagnetic field, electric current, and pressure distributions. In N. Buzulukova (Ed.), *Extreme Events in Geospace* (pp. 259–279): Elsevier. https://doi.org/10.1016/B978-0-12-812700-1.00011-X

Sitnov, M. I., Stephens, G. K., Tsyganenko, N. A., Ukhorskiy, A. Y., Wing, S., Korth, H., & Anderson, B. J. (2017). Spatial structure and asymmetries of magnetospheric currents inferred from high-resolution empirical geomagnetic field models, *Dawn-Dusk Asymmetries in Planetary Plasma Environments* (pp. 199–212). Hoboken, NJ: John Wiley. https://doi.org/10.1002/9781119216346.ch15

Sitnov, M. I., & Swisdak, M. (2011). Onset of collisionless magnetic reconnection in two-dimensional current sheets and formation of dipolarization fronts. *Journal of Geophysical Research*, *116*, A12216. https://doi.org/10.1029/2011JA016920

Sitnov, M. I., Tsyganenko, N. A., Ukhorskiy, A. Y., Anderson, B. J., Korth, H., Lui, A. T. Y., & Brandt, P. C. (2010). Empirical modeling of a CIR-driven magnetic storm. *Journal of Geophysical Research*, *115*, A07231. https://doi.org/10.1029/2009JA015169

Sitnov, M. I., Tsyganenko, N. A., Ukhorskiy, A. Y., & Brandt, P. C. (2008). Dynamical data-based modeling of the storm-time geomagnetic field with enhanced spatial resolution. *Journal of Geophysical Research*, *113*, A07218. https://doi.org/10.1029/2007JA013003

Sitnov, M. I., Ukhorskiy, A. Y., & Stephens, G. K. (2012). Forecasting of global data-binning parameters for high-resolution empirical geomagnetic field models. *Space Weather*, *10*, S09001. https://doi.org/10.1029/2012SW000783

Sorathia, K. A., Ukhorskiy, A. Y., Merkin, V. G., Fennell, J. F., & Claudepierre, S. G. (2018). Modeling the depletion and recovery of the outer radiation belt during a geomagnetic storm: Combined MHD and test particle simulations. *Journal of Geophysical Research: Space Physics*, *123*, 5590–5609. https://doi.org/10.1029/2018JA025506

Speiser, T. W. (1965). Particle trajectories in model current sheets: 1. Analytical solutions. *Journal of Geophysical Research*, *70*(17), 4219–4226. https://doi.org/10.1029/JZ070i017p04219

Stephens, G. K., Sitnov, M. I., Kissinger, J., Tsyganenko, N. A., McPherron, R. L., Korth, H., & Anderson, B. J. (2013). Empirical reconstruction of storm time steady magnetospheric convection events. *Journal of Geophysical Research: Space Physics*, *118*, 6434–6456. https://doi.org/10.1002/jgra.50592

Stephens, G. K., Sitnov, M. I., Korth, H., Tsyganenko, N. A., Ohtani, S., Gkioulidou, M., & Ukhorskiy, A. Y. (2019). Global empirical picture of magnetospheric substorms inferred from multimission magnetometer data. *Journal of Geophysical Research: Space Physics*, *124*, 1085–1110. https://doi.org/10.1029/2018JA025843

Stephens, G. K., Sitnov, M. I., Ukhorskiy, A. Y., Roelof, E. C., Tsyganenko, N. A., & Le, G. (2016). Empirical modeling of the storm time innermost magnetosphere using Van Allen Probes and THEMIS data: Eastward and banana currents. *Journal of Geophysical Research: Space Physics*, *121*, 157–170. https://doi.org/10.1002/2015JA021700

Torbert, R. B., Burch, J. L., Phan, T. D., Hesse, M., Argall, M. R., Shuster, J., et al. (2018). Electron-scale dynamics of the diffusion region during symmetric magnetic reconnection in space. *Science*, *362*(6421), 1391–1395. https://doi.org/10.1126/science.aat2998

Tsyganenko, N. A. (1996). Effects of the solar wind conditions on the global magnetospheric configurations as deduced from data-based field models. In *Proceedings of the Third International Conference on Substorms (ICS-3)* (pp. 181–185). Paris: ESA Publications Division.

Tsyganenko, N. A. (2002). A model of the near magnetosphere with a dawn-dusk asymmetry 1. Mathematical structure. *Journal of Geophysical Research*, *107*(A8), 1179. https://doi.org/10.1029/2001JA000219

Tsyganenko, N. A., & Sitnov, M. I. (2005). Modeling the dynamics of the inner magnetosphere during strong geomagnetic storms. *Journal of Geophysical Research*, *110*, A03208. https://doi.org/10.1029/2004JA010798

Tsyganenko, N. A., & Sitnov, M. I. (2007). Magnetospheric configurations from a high-resolution data-based magnetic field model. *Journal of Geophysical Research*, *112*, A06225. https://doi.org/10.1029/2007JA012260

Vassiliadis, D. (2006). Systems theory for geospace plasma dynamics. *Reviews of Geophysics*, *44*, RG2002. https://doi.org/10.1029/2004RG000161

Wang, C.-P., Lyons, L. R., Nagai, T., & Samson, J. C. (2004). Midnight radial profiles of the quiet and growth-phase plasma sheet: The Geotail observations. *Journal of Geophysical Research*, *109*, A12201. https://doi.org/10.1029/2004JA010590

Wiltberger, M., Pulkkinen, T. I., Lyon, J. G., & Goodrich, C. C. (2000). MHD simulation of the magnetotail during the December 10, 1996, substorm. *Journal of Geophysical Research*, *105*(A12), 27,649–27,663. https://doi.org/10.1029/1999JA000251

Wolf, R. A. (1983). The quasi-static (slow-flow) region of the magnetosphere. In R. L. Carovillano & J. M. Forbes (Eds.), *Solar-Terrestrial Physics* (pp. 303–368). Dordrecht, Netherlands: Springer.

Yao, Z. H., Rae, I. J., Guo, R. L., Fazakerley, A. N., Owen, C. J., Nakamura, R., et al. (2017). A direct examination of the dynamics of dipolarization fronts using MMS. *Journal of Geophysical Research: Space Physics*, *122*, 4335–4347. https://doi.org/10.1002/2016JA023401

Yue, C., Wang, C.-P., Nishimura, Y., Murphy, K. R., Xing, X., Lyons, L., et al. (2015). Empirical modeling of 3-D force-balanced plasma and magnetic field structures during substorm growth phase. *Journal of Geophysical Research: Space Physics*, *120*, 6496–6513. https://doi.org/10.1002/2015JA021226

Zelenyi, L., Artemiev, A., Malova, H., & Popov, V. (2008). Marginal stability of thin current sheets in the Earth's magnetotail. *Journal of Atmospheric and Solar-Terrestrial Physics*, *70*(2–4), 325–333. https://doi.org/10.1016/j.jastp.2007.08.019

Zou, S., Lyons, L. R., Wang, C.-P., Boudouridis, A., Ruohoniemi, J. M., Anderson, P. C., et al. (2009). On the coupling between the Harang reversal evolution and substorm dynamics: A synthesis of SuperDARN, DMSP, and IMAGE observations. *Journal of Geophysical Research*, *114*, A01205. https://doi.org/10.1029/2008JA013449